Master Thesis

Structure and mechanical properties of sputtered AlBN coatings

carried out for the purpose of obtaining the degree Master of Science
under supervision of

Univ.Prof. Dipl.-Ing. Dr.mont. Paul Mayrhofer
Univ.Ass. Dr.rer.nat. Holger Euchner

E308 - Institute of Materials Science and Technology
Faculty of Mechanical Engineering

submitted at

Vienna University of Technology
Karlsplatz 13
1040 Vienna, Austria

by

Pierre Wiehoff
1228339
Lacknergasse 14/12, 1170 Vienna, Austria

Vienna, February 2015

Affidavit:
I declare in lieu of oath, that I wrote this thesis and performed the associated research myself, using only literature cited in this volume.

Date	*Signature*

Contents

Acknowledgements

First of all, i would like to express my deepest appreciation to **Univ.Prof. DI Dr.mont. Paul Heinz Mayrhofer** for giving me the opportunity to write my master thesis within his group. It was a great chance for me to gain a deeper insight into the field of coating development. Furthermore, i would like to thank the whole thin film group for their support and advice in many different ways.

In addition, i would like to thank my thesis supervisor **Univ.Ass. Dr.rer.nat. Holger Euchner** for his guidance and patience during the research process. I am grateful that he expended so much time in the support of my thesis.

I thank all my friends and family members for their encouragement and endorsement.

Abstract

Recently wurtzite boron nitride (w-BN) was proposed to exhibit hardness values higher than diamond. [1] In combination with an excellent corrosion resistance, w-BN would be an ideal material for coatings of cutting tools. However, w-BN has proven to be hardly accessible by standard deposition techniques. Therefore, a possibility to access the properties of w-BN may be the growth of $Al_{1-x}B_xN$ with high boron content, using the assistance of aluminum nitride to promote the growth of the wurtzite structure.

Within this study, we investigated the influence of different boron contents on the w-AlN crystal lattice. Main objective was to show the dependency of the hardness on the boron contents in the coatings. Polycrystalline $Al_{1-x}B_xN$ coatings were grown, using reactive magnetron sputtering with different combinations of 3" and 2", boron and aluminum targets. The deposition was performed at various substrate temperatures in an Ar/N atmosphere. Diverse boron contents were achieved by adjusting the current on the targets. To determine hardness, microstructure and the material contents, the coatings were analyzed by nanoindentation, x-ray diffraction (XRD) and energy dispersive x-ray spectroscopy (EDS).

XRD results have shown, that it was not possible to grow a thin film with over $\sim$10 $at.\%$ boron content in the w-AlN crystal structure. With higher boron contents, the thin films are mostly amorphous with traces of h-BN reflections. The maximal achieved boron content in the amorphous structure was 46 $at.\%$. With w-AlN having hardnesses around 25 GPa, [2] at boron contents of 0-10 $at.\%$, we see a slight raise in hardness up to 30 GPa. At the maximum boron content of 46 $at.\%$, the hardness drops significantly to a minimum of 6 GPa. Coatings consisting of $Al_{x-1}B_xN$ have shown, that high hardnesses only occur in the w-AlN crystal structure.

Kurzfassung

Vor kurzem wurde postuliert, dass wurtzitisches Bornitrid (w-BN) höhere Härten als Diamant haben könnte. [1] In Kombination mit einer exzellenten Korrosionsresistenz, wäre w-BN ein ideales Material für Beschichtungen im Bereich der Schneidwerkzeuge. Jedoch hat es sich herausgestellt, dass w-BN nur sehr schwer herzustellen ist. Eine Möglichkeit das Wachstum von $Al_{x-1}B_xN$ in der wurtzitischen Phase zu begünstigen, ist mit Hilfe von Aluminiumnitrid, welches auch in dieser Phase existiert (w-AlN).

In dieser Arbeit soll der Einfluss vom Borgehalt auf die w-AlN Kristallstruktur und die daraus resultierende Härte untersucht werden. Polykristalline $Al_{x-1}B_xN$ Schichten wurden mit Hilfe eines reaktiven Sputterprozesses beschichtet. Dabei wurden einige Kombinationen aus 3" und 2" Targets, aus Bor und Aluminium verwendet. Der Prozess wurde unter Einfluss von Argon und Stickstoff bei verschiedenen Substrattemperaturen durchgeführt. Um den Borgehalt in den Schichten zu variieren, wurden die Stromstärken schrittweise angepasst. Zur Bestimmung von Härte, Mikrostruktur und Zusammensetzung wurden folgende Prüfverfahren verwendet: energiedispersive Röntgenspektroskopie, Röntgenbeugung und Nanoindentierung.

Die Ergebnisse der Untersuchungen mittels Röntgenbeugung haben ergeben, dass es nicht möglich war, eine Beschichtung herzustellen, die über 10 $at.\%$ Borgehalt hat und die w-AlN Phase besitzt. Bei einem Borgehalt von über 10 $at.\%$, wurden die Schichten amorph und zeigten vereinzelte Reflexionen der hexagonalen Bornitrid (h-BN) Phase. Der höchste Borgehalt wurde mit 46 $at.\%$ gemessen. Auch diese Schicht zeigte nur ein amorphes Muster. Da bei Aluminiumnitrid mit Härten um 25 GPa zu rechnen ist, [2] konnte bei Schichten unter 10 $at.\%$ Borgehalt, ein Anstieg der Härte auf bis zu 30 GPa beobachtet werden. Beim maximalen Borgehalt von 46 $at.\%$ fiel die Härte auf ein minimum von 6 GPa. Es zeigt sich somit eine Abhängigkeit der Härte von der Kristallstrukur , wobei hohe Härtewerte nur bei Schichten mit der w-AlN Phase beobachtet wurden.

1 Introduction

Surface engineering includes a variety of beneficial treatments to alter a materials surface in a desired way. Especially improvements concerning functionality and serviceability are utile in a wide range of applications, such as wear and corrosion resistance of cutting tools. Therefore, techniques for tailoring material properties got a lot more attention in the last decades. Strongly affected by this progression was the field of thin film technology, in which physical and chemical vapor depositions are the essential processes. These processes are crucial when it comes to surface enhancements with respect to high hardnesses, excellent chemical resistance and advanced conductivity of semiconductors. This wide range of possible applications, makes them ideal for aerospace, automotive, electronic and machining industries, and subsequently an interesting field of research. [3, 4]

Diamond is known to be the hardest material discovered so far. In the last decades extensive theoretical and experimental efforts have been made, to find materials with comparable hardness and better thermal stability. A recent report shows that a nano-composite, including a mixture of cubic (c-BN) and wurtzite boron nitride (w-BN), is able to reach the same indention hardness as diamond. [1] While c-BN is well known as the second hardest material, it is still less hard and stable in comparison to diamond. Surprisingly, theoretical predictions suggest, that w-BN may be even harder than diamond, which does not cohere to the similar elastic moduli, bond lengths, shear and tensile strengths of w-BN and c-BN. The idea behind this work is to grow w-$Al_{x-1}B_xN$ with high boron content using aluminum nitride to promote the growth of the wurtzite structure. [5, 6, 7]

Main goal of this work is to achieve the growth of boron rich $Al_{x-1}B_xN$ in its wurtzite phase, with the help of AlN. The fact that AlN is stable in the wurtzite phase, leads to the conclusion, that adding of boron might result in the growth of w-BAlN with enhanced mechanical properties. With physical vapor deposition (PVD), coatings consisting of the ternary system $Al_{x-1}B_xN$, are grown on a substrate. The deposition was performed with various parameters to achieve the growth of samples with different boron contents. These samples (substrate and coating) are then investigated by x-ray diffraction, energy dispersive x-ray spectroscopy and nanoindentation, to identify trends in hardness and crystallography. This may lead to the detection of advanced material properties.

2 Theoretical framework

2.1 Surface engineering

Altering surface properties can lead to a variety of benefits in different applications such as hard coatings for instruments, optical coatings, coatings for electronic devices and coatings with decorative purposes. There are two particular processes in surface engineering, overlay and modification. Adding matter by depositing atom-by-atom and covering the underlaying specimen (substrate) is called overlay process. Exemplified by the introduction of carbon or nitrogen into a steels surface, to harden or dope semi-conductors for enhanced conductivity. Adapting the surface materials properties is called modification process. As for instance, the application of high hardness coatings to tools, like Aluminum on a polymers surface. It is also possible to perform a pre-modification of the surface properties, followed by an overlaying of the substrate with a coating or a thin film afterwards. In general, atomistic depositions, that have thicknesses around a micron or less (1 micron = 10^{-6} m), are called thin films. Those with higher thicknesses are called coatings. The properties of thin films and coatings are mainly affected by the substrate and the process environment (e.g. vacuum, gaseous, electrolytic or plasma).[8]

2.1.1 Thin films

Growth of thin films is mainly driven by evaporation of a solid material in an vacuum environment. This can be obtained by heating, ion sputtering or an arc discharge. Fig 2.1 shows the deposition of atoms on a substrate. Starting with random nucleation, which results in nucleation growth stages, that rely on various deposition conditions, such as temperature and substrate composition. Furthermore, crystal phase and orientation also depend on these deposition conditions. Nucleation stages can be modified by external forces, such as ion bombardments. An important guideline for systematizing the relation of experimental results and dependence on the deposition temperature (T_s/T_m, where T_s represents the substrate temperature and T_m the melting point of the material) gives the structure zone model (SZM).

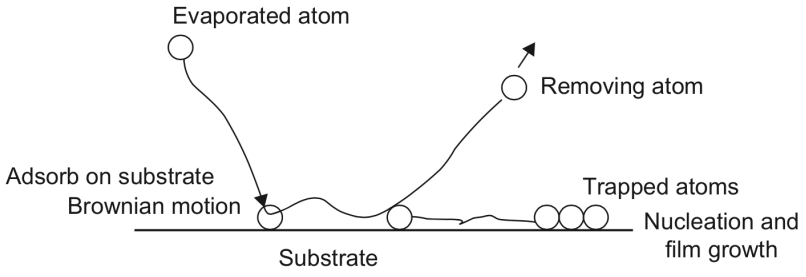

Figure 2.1: Schematic drawing of a typical nucleation and growth process, including adsorption and removing (deflection) of evaporated atoms. [10]

Due to the synthesization from ultra fine particles (e.g. atoms) , thin films have the possibility to form very uniform compounds. These compounds can not be found in bulk materials,

which are usually synthesized by sintering processes, when it comes to boride and nitride materials.

2.1.2 Nucleation and growth of thin films

Growth of thin films, which proceeds through various consecutive stages, can be described by different processes of structural evolution: Nucleation, island growth, coalescence of islands, formation of polycrystalline islands and channels, development of continuous structure and thickness growth. In the nucleation phase, condensation (primary nucleation) starts the film growth on the whole substrate surface simultaneously. Later on, liquid like coalescences (secondary nucleation) are developed. The secondary nucleation starts the local growth subsequently. It is important to mention, that on amorphous substrates, the nucleation starts in random directions. Crystal growth describes the forming of structures in the condensed phase by depositing further material. There are basically two ways of crystal growth on the surface, discrete crystal dispersion and growth of polycrystalline structures. Dispersed crystals grow in random directions, due to the random orientation of the nuclei. Grain coarsening is a result of complete coalescence of crystals, which also leads to formation of discrete single crystals and changes in the orientation by reason of minimization of substrate-crystal interface energy.

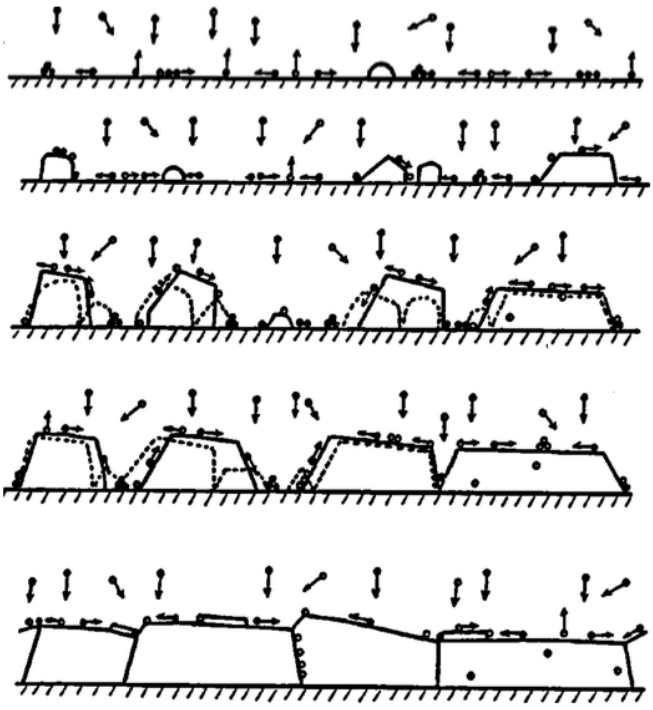

Figure 2.2: Schematic drawing of the growth process of thin films [14]

A Polycrystalline structure consists of various crystals with different orientations, grain sizes and surface conditions. These determinants will influence the behavior of the polycrystalline

film. Slow growing crystals will be overgrown by faster ones in the direction of the crystal faces, which are orientated away from the substrate - the so called competitive growth. The overgrown crystals develope v-shape grains.This leads to a different morphology and texture throughout the film thickness, beginning with random orientation near the substrate surface, followed by v-shaped grains and preferentially oriented crystals. [13, 14, 15]

2.1.3 Structure zone models

Due to the fact that polycrystalline thin films have a great variety in morphology, structure and orientation of crystals, the introduction of structure zone models (SZM) is necessary. [16, 18] They represent a guideline for experimental results, as well as the dependency on the deposition temperature (T_s/T_m) of the structure. As shown in Fig 2.3, the structure zone models are separated into different zones, which can be characterized by their texture.

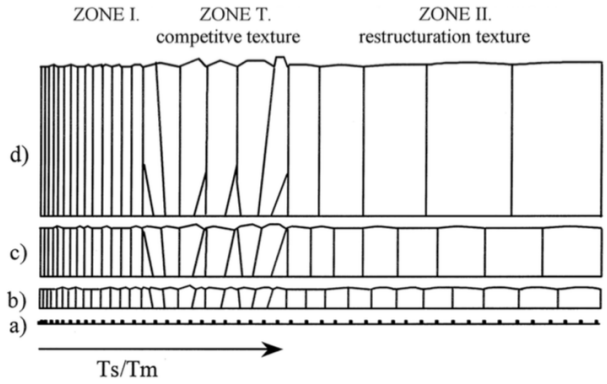

Figure 2.3: SZM at different film thicknesses [14]

The composition of the film in zone I ($0 < T_s/T_m < 0.2$) is governed by statistical fluctuation and nucleation density. The crystalline fibers grow homogeneously away from the substrate surface to the top of the film. The fiber diameter raises with increasing temperature (T_s/T_m), while the crystals have high density of defects and porous grain boundaries. In the temperature range of zone I, bulk diffusion and self surface diffusion are irrelevant. Zone T ($0.2 < T_s/T_m < 0.4$) is dominated by an inhomogeneous structure, that is fine crystalline near the substrate surface and forms v-shaped grains through the thickness, ending in columnar shape at the film surface. In this zone, self service diffusion is present and grain boundary migration is narrow. In zone II ($0.4 < T_s/T_m$) the structure becomes homogenous again and consists of nearly perpendicular (to the film plane) columns. In real deposition processes impurities are hardly avoidable, which leads to the formation of surface covering layers (SCL). These layers cover the surface of the crystal and its grain boundaries, that directly effects the crystal and grain growth by rounding and truncation of the crystal shape. Complete surface covering causes fully blocking of the crystal and leads to repeated nucleation as the condensation proceeds.

2.2 Physical vapor deposition (PVD)

Physical vapor deposition is an operation, where a solid or liquid material is vaporized into atoms or molecules. These particles are then transported through a vacuum or plasma environment and condense at the substrate surface. Common deposition rates range from 1 to 10 nm/s but are strongly dependent on the process. A reactive deposition can be used for compound material creation. The evaporated material reacts with ambient gas to form a new composition. For example, vaporization of aluminium in an nitrogen environment, resulting in the formation of aluminium nitride. It is also possible to perform a deposition from a compound source material called quasi-reactive deposition. Due to the loss of a less reactive species, a partial pressure of reactive gas for compensation is introduced (Boron nitride in nitrogen). The three main PVD groups are vacuum evaporation (a), sputter deposition (b,c), cathodic arc (d), ion plating (e,f,g) and ion beam-assisted deposition, IBAD (h). [8]

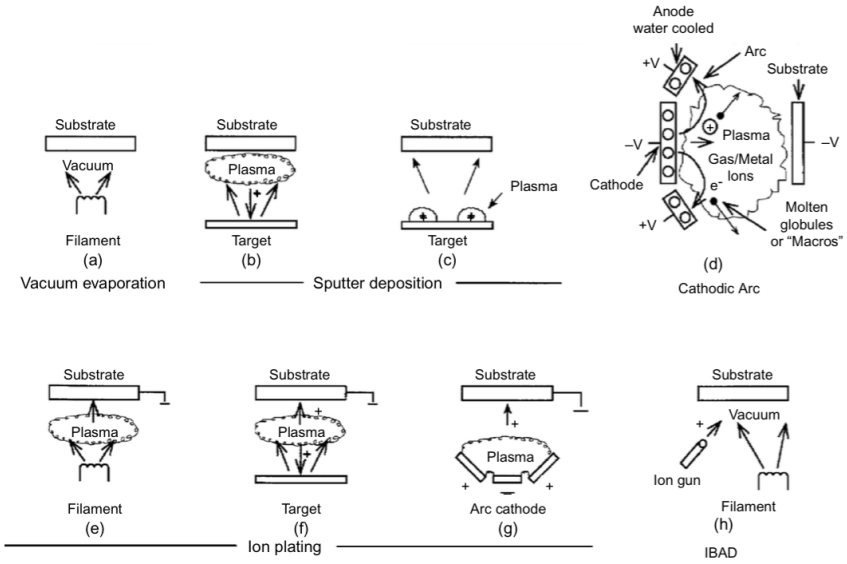

Figure 2.4: PVD categories [8]

2.2.1 Sputter deposition

Sputter deposition, often just called sputtering, refers to the deposition of evaporated particles from a materials surface (target) by a non-thermal vaporization process. In this process atoms are dissolved from the solid surface by momentum transfer from bombarding particles. Usually this particle is an out of plasma accelerated gaseous ion. The ion is a result of the collision of an electron with the ambient gas (working gas). This collision leads to the ionization of the gas atom, going along with the creation of a free electron. This interaction, with argon (Ar) being the ambient gas, can be described by the following equation:

$$e^- + Ar = Ar^+ + 2e^- \tag{2.1}$$

The free electron is then a source for further collisions, resulting in a chain-like process. Due to the high potential difference between the substrate (anode) and the target (cathode), gas ions are then accelerated towards the target . At the target surface the ions eject solid source material atoms (usually metals) by collision. These ejected atoms are then transferred to the substrates surface, where they form a thin film by condensation. Most essential parameter of sputtering processes is the sputtering yield Y, representing the ratio of ejected atoms at the target and the incident ions on the substrate. Y is mainly influenced by the incident ion energy, their incidence, as well as mass and binding energy of the target atoms. Fig 2.5 shows a typical setup for a sputtering process.

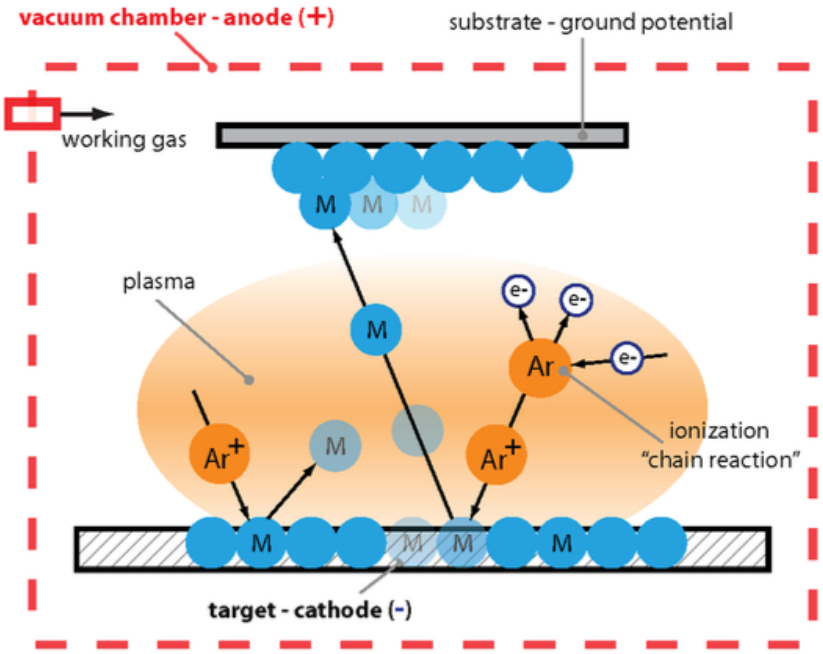

Figure 2.5: Schematic drawing of a sputtering process, showing the chain reaction in the plasma environment. [9]

Due to the fact that plasma consists of charged particles, the presence of a magnetic field improves deposition efficiency. The magnetic field is usually introduced at the target in order to achieve a higher local ionization and particle density, while evaporating. This technique is called magnetron sputtering. Heating of the cathode is another approach to improve the sputtering yield. Depending on the material, the activation energy on the substrate surface is decreased. In comparison to vacuum deposition processes, the distance between target und substrate is short. Sputter deposition can be performed in low pressure plasma ($< 5mTorr$) or by the use of an ion gun. The absence of particles in the low pressure plasma leads to the advantage, that fewer collisions between sputtered and gaseous particles occur. The plasma is usually established in the area between the target and the substrate or near the target surface.

Sputtering can be performed with a direct current (DC) or a pulsed current. While DC is the most efficient technique in sputtering technology, it is limited to conductive materials. Operating with non-conductive materials requires a pulse controlled process, avoiding electrostatic

charge. This is accomplished by the introduction of short rejective pulses (positive) followed by long negative pulses. Another problematic issue of DC sputtering with non-conductive materials is arcing. Arcing is a high current, low voltage discharge inside the chamber that can only be countered by generators with included arc suppression units. [8, 10, 11]

2.2.2 Vacuum deposition

Vacuum deposition, also known as vacuum evaporation, is a thermal evaporation process. The absence of working gas causes the particles to reach the substrates' surface with almost no interactions and/or collisions with gas molecules (depending on vacuum quality). Desirable gas pressures range from 10^{-5} to 10^{-9} $Torr$ ($1\ Torr \approx 1333.32\ \mu bar$). Depending on the tolerated gas contamination level, high evaporation rates are possible. Demanding higher purity of the thin films, better vacuum is needed. Thermal evaporation of a source material can be achieved by thermal heating of adjacent parts (e.g. tungsten wire coils) or by heating the source material itself (e.g. by electronic beam). Since the substrate is at much lower temperature, the high energy molecules will move to the substrate surface, transfer their energy and condense. To reduce heating of the substrate, an appreciate distance from the heating source is necessary. Thermal evaporation is usually used for optical interference coatings, mirror coatings, decorative coatings, wear resistance coatings and protective coatings.

2.2.3 Cathodic arc

Cathodic arc or arc vapor deposition is a process, where the source material is vaporized by a high current, low voltage electrode or anode (anodic arc), resulting in high ionization. With a biased substrate, ions are easily accelerated to the substrate surface. Arc vapor deposition is mostly used for hard, decorative coatings and ion plating processes.

2.2.4 Ion plating

For a better control of the deposition, ion plating (or ion-assisted deposition - IAD) uses a concurrent or periodic bombardment of atomistic particles to change the properties of the film on a substrates surface. Most important process variables for the ion bombardment are flux, energy, mass and particle ratio (bombardment/deposition). Evaporation and sputtering are viable processes for the material deposition. Particles used for ion plating arise from the reactive gas or the condensing material itself (film ions). The process can be executed in a plasma environment as well, in which a separate ion source is needed (e.g. ion gun) . This operation is usually called ion beam-assisted deposition (IBAD). It is also possible to use compound materials as source by introducing a reactive gas into the plasma. Ion plating is the operation of choice for depositions with a high demand of density that usually leads to hard coatings.

2.3 Nitride coating systems

Nitrides are chemically bondings of nitrogen with other materials (metals and metalloids). They are used as a compound material in a large variety of applications. Like carbides, nitrides are often used as refractory material, due to their high lattice energy. Especially group III nitrides (e.g. AlN, BN or GaN) offer plenty of good properties, like thermal stability, good thermal conductivity and mechanical strength (e.g. high hardness). Nitride compounds can be used for hard coatings, high temperature applications and insulators as well as semiconductors. [19]

2.3.1 AlN - Aluminium nitride

Aluminium is the earths' most abundant metal and a chemically very reactive material. It has an outstanding low density and corrosion resistance. Aluminum is highly reactive with oxygen, building a passivation layer of aluminum oxide when exposed to air. Its low density and durability makes it an ideal metal for light weight purposes such as aerospace engineering. The crystal structure of aluminum is face-centered cubic (fcc) at room temperature and atmospheric pressure.
An interesting aluminium compound is aluminium nitride (AlN). Aluminium nitride comes in two different phases, wurtzite (w-AlN) and cubic (c-AlN). w-AlN is a modification of the hexagonal phase, which provides a wide band gap and high hardnesses, making it relevant for a large field of applications, such as insulating and passivating layers, acoustic wave devices and tribology. Ternary systems, such as $Ti_xAl_{x-1}N$, which crystalize in the cubic phase (c-AlN), offer a variety of features including mechanical strength, chemical resistance and thermal stability. [20] Fig 2.6 and 2.7 show the unit cell, as well as the crystal structure of w-AlN (the large blue atoms representing Al). [21]

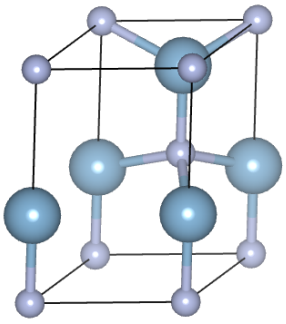

Figure 2.6: Unit cell of w-AlN

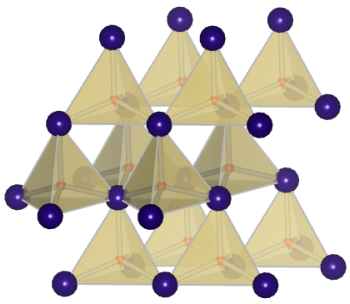

Figure 2.7: Crystal structure of w-AlN

The properties of AlN strongly depend on the crystal structure (c-AlN, w-AlN), grain size and orientation. In PVD processes, these properties can be adjusted by alloying of different elements as well as the regulation of the ion bombardment of the growing film. Fig 2.8 shows the mechanical properties and lattice constants of wurtzite aluminium nitride.

Type	Hardness (GPa)	Modulus (GPa)	Lattice constant (nm)
h-BN	11.5–12.9	200–253	a=0.2504, c=0.6660
c-BN	30–50	794–900	a=0.3615
w-BN	27	790–831	a=0.2553, c=0.4228
w-AlN	26	240	a=0.3111, c=0.4979

Figure 2.8: Mechanical properties and lattice parameters of bulk AlN and BN. [26]

2.3.2 BN - Boron nitride

Boron is an element, that is entirely produced by cosmic ray spallation and has a low abundance in the earth's crust. It is very hard to produce pure boron, due to its tendency to form refractory materials (e.g containing carbon). Boron is capable of forming stable covalently bonded molecular networks. [22] Crystalline $\alpha-$boron is very hard (up to 58 GPa *Vickers hardness*) and has a melting point of 2349 K. It is commonly used in glass and ceramics as a compound, enhancing strength and fluxing qualities. Its ability to increase micro-hardness and surface resistance, by introduction into other metals, makes boron a very attractive material for physical vapor deposition purposes. [23]
Especially boron nitrides are an interesting field of research, due to excellent mechanical properties. As shown in Fig 2.9-2.11, [21] boron nitride exists in a cubic (c-BN) and two hexagonal modifications (h-BN and w-BN), where h-BN is the more stable phase (larger green atoms representing B). Boron nitride builds strong covalent bonds within a layer like structure. Between the different layers, the weak van der Waals forces are dominant. In c-BN and w-BN, both boron and nitrogen show tetrahedral coordinations, but have different angles. c-BN is known to exhibit ultra high hardnesses. Lattice parameters and mechanical properties of the different BN phases are shown in Fig 2.8. There is also a wurtzite form of BN (w-BN), which may be even harder than c-BN, but very difficult to synthesize. [24, 25]

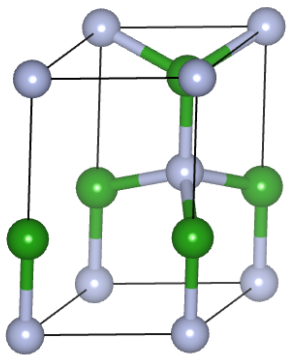

Figure 2.9: Tetrahedral coordinated w-BN

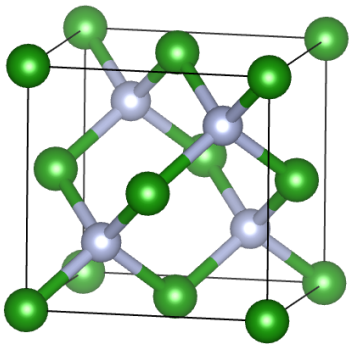

Figure 2.10: Tetrahedral coordinated c-BN

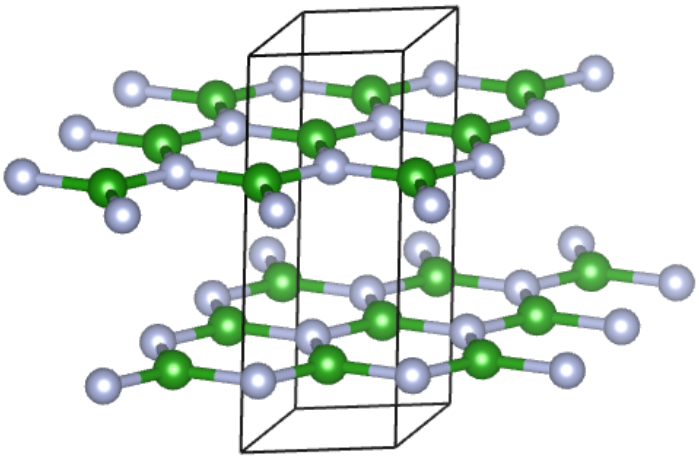

Figure 2.11: h-BN

3 Analysis

3.1 Hardness tests

Hardness is the resistance of a material against the indentation of another, harder material. In most cases this deformation is strongly localized (small dents or scratches). Hardness measurements after Mohs were one of the early hardness tests at the beginning of the 20th century, where the ability of one mineral to scratch another softer mineral was measured. The Mohs scale was then introduced, ranging from 1 to 10, in which 1 is a very soft material and 10 is diamond. Over the years more quantitative techniques for hardness measurements have been developed, where small indenters are forced into a materials surface. Depth and size of the resulting indentation leads then to the output of a specific hardness number - a low hardness number for soft materials with deep and large indentations and a high number for harder materials with low indentation depths. Hardness measurements are always considered with respect to each other (diamond as the highest) and should be treated carefully. Hardness tests are the most frequent tests done in mechanical analysis due to their effectiveness and simplicity. [12]

3.1.1 Rockwell hardness test

Because of their simple execution, hardness tests after Rockwell are the most commonly used methods for hardness measurements. Virtually all materials and even some polymers can be tested, due to the large variety of indenters and their scales. Indenters for the Rockwell test are spherical and hardened steel balls with diameters ranging from 1.588 mm to 12.7 mm. Even the hardest materials can be measured, using a conical diamond called *Brale indenter*. As shown in Fig 3.1 the test is performed in three steps, which involve indentation of a minor load F_0 followed by a large major load F_1 and unloading (only F_1).

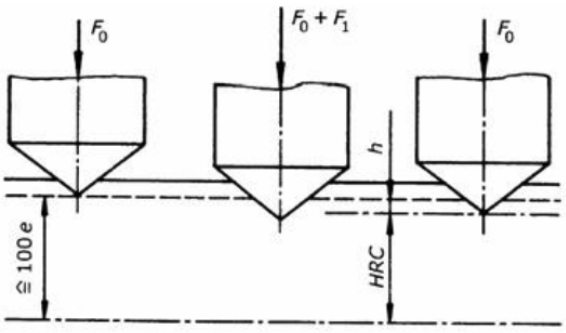

Figure 3.1: Principle of Rockwell hardness [27]

The difference in indention depths determines the hardness. Using an initial minor load enhances the test accuracy. There exist different Rockwell setups with different indenters. Fig 3.7 gives an overview of the test methods depending on load and indenter type.

Scale symbol	Penetrator	Major load (kg.)	Dial number
A	Diamond	60	Black
B	1/16-inch ball	100	Red
C	Diamond	150	Black
D	Diamond	100	Black
E	1/8-inch ball	100	Red
F	1/16-inch ball	60	Red
G	1/16-inch ball	150	Red
H	1/8-inch ball	60	Red
K	1/8-inch ball	150	Red

Figure 3.2: Notation of the Rockwell test methods with different loads and indenters (diamond cones ans steel balls)

For all Rockwell tests minor load is 10 kp. Tests with a steel sphere (ball) are usually carried out for softer materials, while diamond cones are used for harder specimens. Rockwell hardness measured with diamond cones is defined by following equation, where t is the indentation depth:

$$HR = 100 - \frac{t}{0.002mm} \tag{3.1}$$

And for Rockwell test with steel sphere, the following equation defines the hardness:

$$HR = 130 - \frac{t}{0.002mm} \tag{3.2}$$

There are also superficial Rockwell tests with minor loads (3 kp), especially made for thin specimens, that can not carry extensive loads. An example for notation of Rockwell hardness tests is 60HR30W. Each load represents a scale, followed by a letter depending on the indenter type - where 60 is the hardness, HR stands for Rockwell hardness, 30 is the scale (30 kp) and W the indenter model. Hardness values should always range between 20 to 100, where they are accurate. Beneath 20 or above 100 the next softer or harder scale is needed to get valid data. [12, 27, 28]

3.1.2 Brinell hardness test

Like the Rockwell treatment, Brinell hardness test involves an indentation with a hard and spherical indenter. There are different indenter diameters (1 mm, 5 mm and 10 mm) and loads (ranging from 500 kp to 3000 kp in 500 kp steps). While the test is running, the load remains constant for a specific period of time (10 to 30 s). The harder the specimen, the greater the required load. The Brinell hardness number (HB) is a function of the load (P) and the diameter (d) of the indentation as well as the diameter of the indenter (D):

$$HB = \frac{2P}{\pi \cdot D(D - \sqrt{D^2 - d^2})} \tag{3.3}$$

The diameter of the indentation is usually measured via low-power microscope with an attached scale to determine the remaining indent. An example for the standard Brinell hardness notation is $400HBW10/3000$. HBW indicates that a 10 mm - diameter steel ball was used as indenter, with a load of 3000 kp. The hardness of the specimen in this notation is 400. For extremely hard materials a tungsten carbide ball is needed as indentation tool. [29]

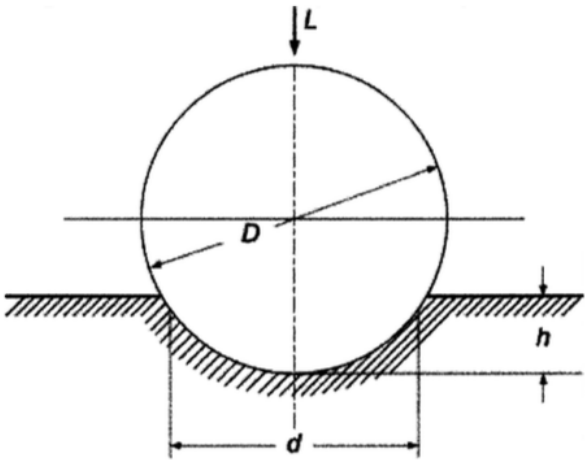

Figure 3.3: Principle of Brinell hardness test with the applied force L, the indenter diameter D and the indentation diameter d. [29]

3.1.3 Vickers and Knoop hardness test

In comparison to Rockwell hardness test, Vickers and Knoop (and Brinell) use the remaining area of the indentation and not the remaining depth of indentation for hardness determination. The hardness test involves a small diamond indenter that has a pyramid like shape. A Knoop indenter has two different side length, with l being the longer part (see Fig 3.4). If the measured diagonals d of the remaining indentation area, caused by the Vickers pyramid, are not even, the arithmetic average of both has to be calculated. The indenter is forced into the specimens surface with a much smaller load as compared to Rockwell or Brinell. The applied load P ranges from 0.2 to 10 kp. The resulting indentation is then measured with the assistance of a microscope and converted to the hardness number (HV Vickers, HK Knoop).

$$HK = 14.2 \cdot \frac{P}{l^2}; \tag{3.4}$$

$$HV = 1.854 \cdot \frac{P}{d^2} \tag{3.5}$$

In this testing process, it is important to have a well prepared and clean surface (polishing) to ensure accurate measurements. Due to the low indentation depth, Vickers and Knoop tests are often called micro-indentation tests and are accurate choices for smaller specimen, as well as brittle materials like ceramics.

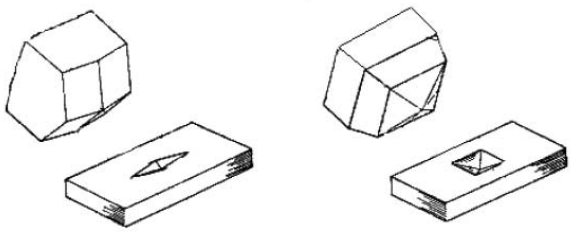

Figure 3.4: Principle of Knoop (left) and Vickers (right) tests, showing both indenters and resulting indentation marks. [30]

Vickers tests are normally independent from the magnitude of the load. As an example how Vickers hardness numbers can be reported, serves the notation $300HV10/20$ (300 being the hardness number, HV for Vickers scale, 10 the applied load in kp and 20 the loading time).

3.1.4 Nanoindentation

Nanoindentation is a method that uses penetration depth along with the applied load to measure hardnesses of a specimen, especially thin films. It is also possible to measure other mechanical properties with this technique, such as the elastic modulus, fracture toughness and yield strength. The most popular testing geometry is the three-sided Berkovich indenter, that is shown in Fig 3.5. The Berkovich indenters face half-angle is $\phi = 65.27°$. This yields approximately the same projected area as for Vickers indenters.

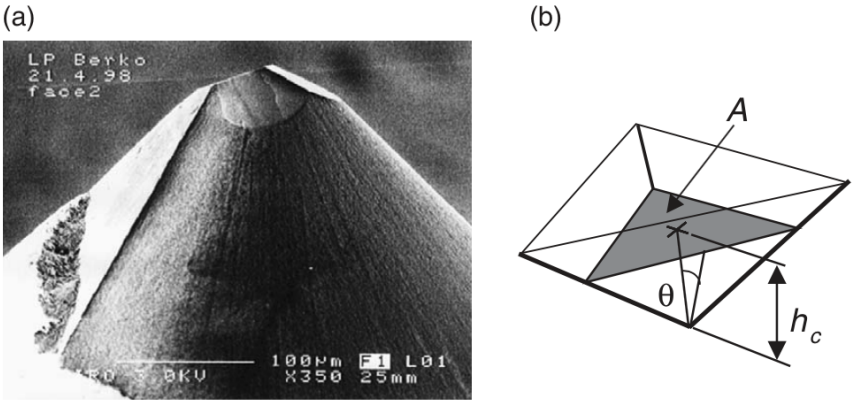

Figure 3.5: High magnification of a Berkovich diamond nanoindenter (a) and its geometry (b) [32]

The projected area is observed when looking face-on to the residual impression of the specimens surface, without paying attention to the sloping sides of the penetration. The advantage

of a three-sided Berkovich indenter over an indenter that is used in other hardness tests (e.g. Vickers), is the sharper tip, when the indenter is well ground. The tip of a four-sided indenter always has an undesirable line of conjunction, making the Berkovich indenter a tool that grinds easier into a materials surface. The Nanoindentation process involves introduction of a load to the specimen for a certain period of time, followed by a hold and unload period, depending on the material of the specimen. Loading and unloading periods are defined by the user in advance. A polymer needs a longer hold period, because of its significantly longer creep time. Most important test parameter is the load-displacement curve (P-h-curve), which has a different appearance with changing material, reflecting different properties. Fig 3.6 shows a typical load-displacement curve of an elastic-plastic material, where P designates the applied load and h the relative displacement to the initial surface (undeformed). [31, 32]

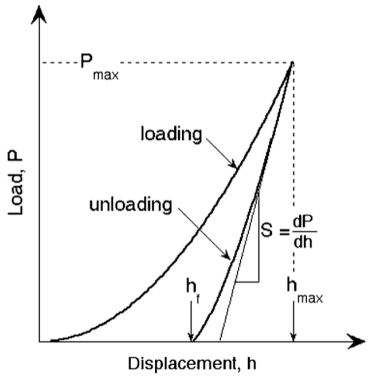

Figure 3.6: P-h-curve of a single crystal showing loading and unloading curves to determine the elastic unloading stiffness S. [34]

Deformation is considered to be elastic and plastic at loading. At unloading only the elastic displacements are recovered, which is important for the analysis of the materials facilitates. Quantities that are measured from P-h-curves are maximum load P_{max}, maximum displacement h_{max}, the final depth h_f and the elastic unloading stiffness $S = dP/dh$. The accuracy of the test depends on how well these parameters can be determined in the experimental environment. Fig 3.7 shows the exact unloading process to measure the hardness H of the specimen. [33, 34]

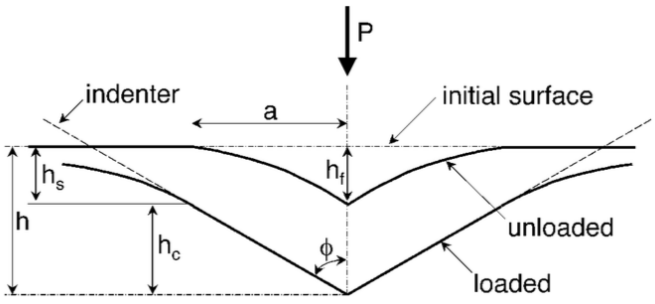

Figure 3.7: Unloading procedure and parameters characterizing the geometry, like maximum load P_{max}, vertical displacement h_c, sink-in h_s and final depth h_f. [35]

With assuming that pile-up at the contact periphery is negligible, the amount of sink-in h_s can be evaluated by following equation (after Oliver and Pharr to fit P_{max} [34, 35]):

$$h_s = \epsilon \cdot \frac{P_{max}}{S} \tag{3.6}$$

$$\tag{3.7}$$

Where ϵ is a geometry constant of the indenter, that is used in the test (e.g. $\epsilon = 0.75$ for paraboloid or $\epsilon = 1$ for flat punch). Fig.3.7 shows the dependence of the vertical displacement h_c from the amount of sink-in, which can be determined as:

$$h_c = h_{max} - \epsilon \cdot \frac{P_{max}}{S} \tag{3.8}$$

To describe the projected area of the indenter, an area function $F(d)$ is introduced. Assuming that the length d is the distance to the tip, the contact area A is given by $A = F(h_c)$. This function has to be calibrated by independent tests to take the deviations of the optimal indenter geometry into account. Usually fused silica is used for these tests. After determining the contact area, the hardness can be estimated: [34, 35]

$$H = \frac{P_{max}}{A} \tag{3.9}$$

3.2 X-ray diffraction (XRD)

X-Ray diffraction is a crucial tool for identification and characterization of materials, like minerals, metals and ceramics. Crystalline materials can be characterized by their chemical composition and the arrangement of their three-dimensional structure of atoms. The smallest structural unit inside a crystal is called a unit cell and contains all the chemical and structural information. A crystal structure consists of three dimensional arrangements of these unit cells. A unit cells physical dimension is represented by the lengths of the cell edges ($\vec{a}$, $\vec{b}$, $\vec{c}$) and the angles between them (α, β, γ). These parameters are called lattice parameters or lattice constants. The atoms within a unit cell are expressed by fractional coordinates that are relative to the length of the unit cell. Unit cells have lengths of several Ångström Å(1 Å= $10^{-10}m$). Considering that crystals have sizes of microns, they consist of billions of unit cells, that are arranged periodically.
Diffraction occurs when x-rays interact with these periodic crystal structures. X-rays are electromagnetic waves with wavelengths of about 1 Å. These waves introduce electric fields, which interact with the electron distribution of an atom. This interaction leads to the emission of photons with wavelengths equal to the incident radiation. Depending on the number of electrons (atomic number), the ability to scatter varies through different atoms. Atoms with high atomic number have better scatter ability than atoms with only a few

electrons. The amplitude of the scattered radiation is directly proportional to the atomic number and is called form factor f_n. As inferred from Fig 3.8, the form factor and the resulting amplitude of the outgoing radiation also depends on the scattering angle 2Θ.

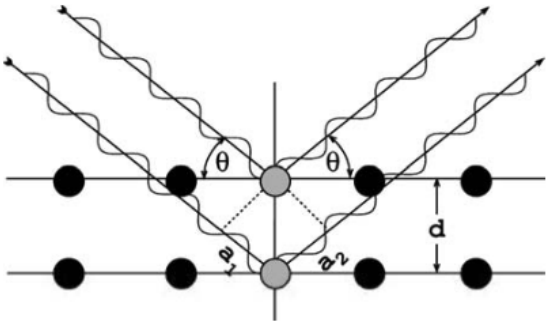

Figure 3.8: Scattering of x-ray beams at adjacent lattice planes leading to constructive interference as an integer multiple of the wavelength λ. [36]

Diffraction causes redistribution of intensities into certain directions, leading to intensity maxima and minima. As can be seen in Fig 3.8, parallel waves that are reflected at adjacent lattice planes, accumulate a path difference $(2 \cdot d \cdot sin\Theta)$. Depending on the path difference, constructive interference is obtained, when the following equation is fulfilled: [37]

$$n \cdot \lambda = 2 \cdot d \cdot sin(\Theta) \tag{3.10}$$

This equation is called Bragg equation, with λ being the radiations wavelength, Θ the angle between planes and incoming radiation (Bragg angle), and d the distance between adjacent lattice planes. With respect to Bragg's law, the peaks of the measured XRD data are used to identify the material and crystal structure. Fig 3.9 shows a typical XRD diagram.

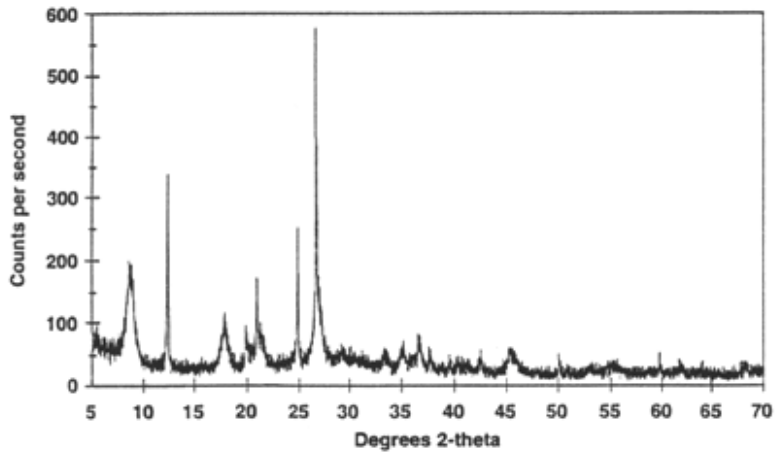

Figure 3.9: XRD diagram: counts per second over 2Θ

Even small deviations from the Bragg angle lead to cancellation by interference, resulting in sharp peaks. This is not the case for small crystal sizes. The dependence of the interference from the crystal size is given by the interference intensity equation, where N represents the number of unit cells and h the reflection index:

$$S = \frac{(sin\pi hN)^2}{N \cdot (sin\pi h)^2} \tag{3.11}$$

Fig 3.10 shows the distribution of the interference equation against the continuous variable h. The interference function has to be calculated individually along the axis for x, y and z. The results are then multiplied and give the interference function for the crystallite. Broad peaks indicate small crystals while large crystals are generally responsible for sharp peaks.

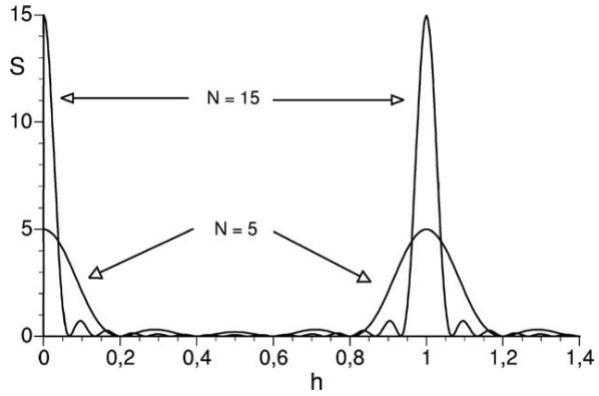

Figure 3.10: Interference function S with continuous variable h (for N=15 and N=5). [36]

Each structure or phase shows distinct diffraction patterns, with characteristic peaks and relative intensities. This is a direct outcome of different amplitudes and relative phases. Combining these parameters leads to complex numbers. Simply adding all complex numbers from different atom positions and amplitudes leads to the introduction of the structure factor F:

$$F(hkl) = \sum f_n exp(-i\Phi_n) = \sum f_n(cos\Phi_n + isin\Phi_n) \tag{3.12}$$

The atom form factor f_n is calculated over all atoms n. The angle Φ_n is given by multiplication of the fractional coordinates x_n, y_n and z_n ,with the Miller indices h, k and l of the respective lattice plane: [36, 37, 38, 39]

$$\Phi_n = 2\pi(hx_n + ky_n + lz_n) \tag{3.13}$$

3.3 Energy dispersive x-ray spectroscopy (EDS)

Energy dispersive x-ray spectroscopy is an operation to distinguish the chemical composition of a material. An electron from a radiation source, like a scanning electron microscope (SEM), causes an electron from an inner shell of an atom to eject. This leads to a hole in the shell, that is filled by an electron of a higher energy level. To fit the gap in the shell, the electron has to release some of its energy, in form of electromagnetic radiation. The released energy is equal to the difference between the energy levels of the electrons of the respective cell. Electromagnetic radiation can be classified by its wavelength. Planck's Equation shows the relation between energy E and wavelength λ of a photon:

$$\lambda = \frac{hc}{E} \tag{3.14}$$

where c is the speed of light and h Planck's constant. Because of the large difference in energy, the emitted radiation appears mostly in the form of x-rays. Fig 3.11 shows the interactions of the emitted electron and the shells (energy levels) of an atom.

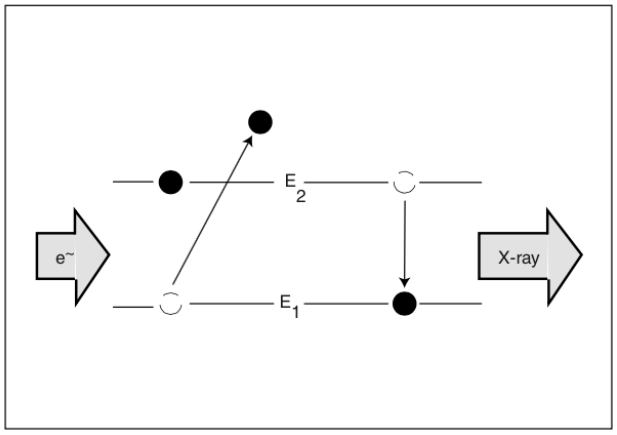

Figure 3.11: (1) Dislodging of an electron of low energy E_1 by an energetic electron e^-. (2) Filling of the gap by an electron from a higher energy level E_2. (3) Emission of radiation in form of x-rays. [40]

Any element, that is excited by electrons of sufficient energy, emits a unique pattern of x-rays. Counting the number of emitted x-rays at a certain energy, with the help of a semiconductor detector, can be used to determine the exact concentration. As shown in Fig 3.12, the collected data produces an x-ray spectrum of the material, showing all detected elements. [40]

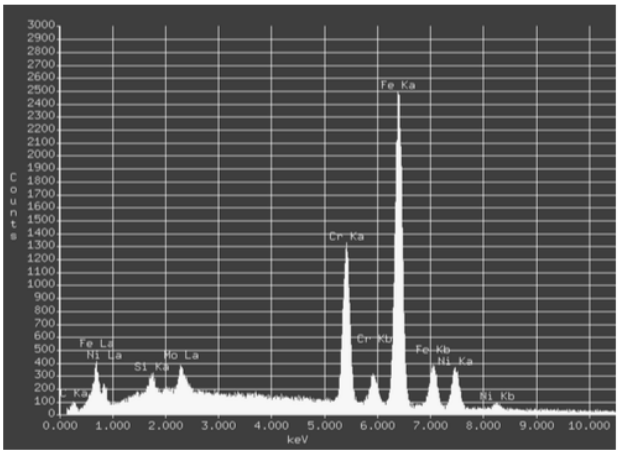

Figure 3.12: Typical EDS spectrum, including major spectral peaks [40]

3.4 Ball crater test

Ball crater test, also called calotest, is a simple and quick method to determine thicknesses of thin films and coatings. In this process, a rotating sphere (e.g. steel ball), which position remains constant, is pressed on the specimen. The steel ball is covered with an abrasive diamond suspension, which leads to grinding of a spherical calotte into the specimen, with the same geometry as the ball.

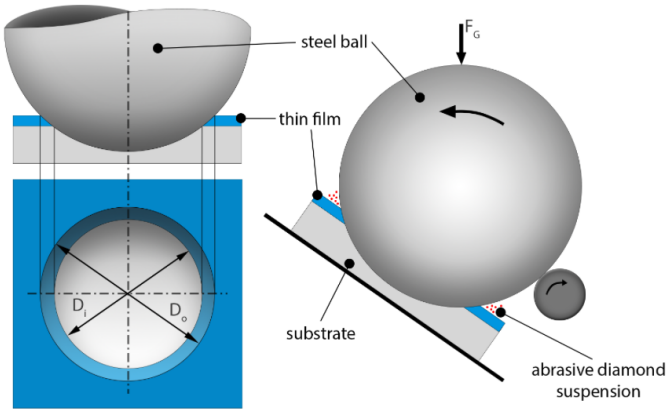

Figure 3.13: Principle of a ball-crater-test with a rotating steel ball. [41]

Fig 3.13 shows the principle of the ball-crater-test, with F_G representing the gravimetric force, d the diameter of the steel ball, D_i the inner diameter and D_o the outer diameter of the spherical depression. The thickness t of the layer is then determined by the following equation:

$$t = \frac{(D_o^2 - D_i^2)}{8 \cdot d} \tag{3.15}$$

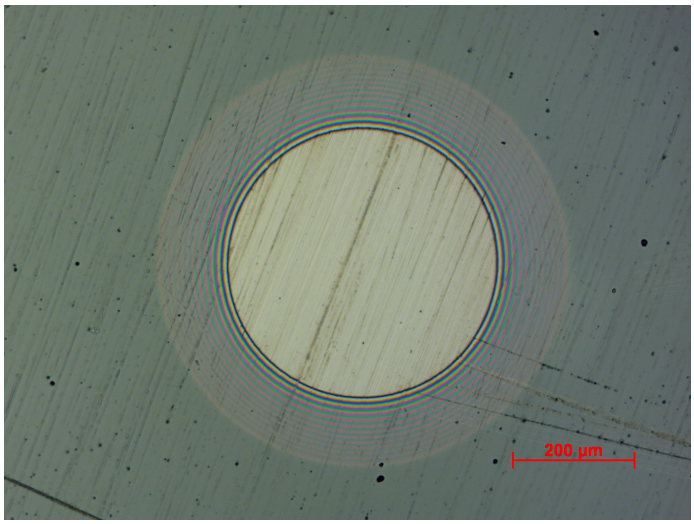

Figure 3.14: Typical image of a spherical depression from a ball crater test, taken with a Zeiss AxioCam ERc 5s attached on Zeiss Axio Lab.A1 microscope.

4 Experimental

Main objective of this work was to achieve the growth of $Al_{1-x}B_xN$ coatings in the hexagonal wurtzite phase with high boron content. The fact that there exist experimental reports on a wurtzite phase of AlN and BN (w-AlN and w-BN), leads to the conclusion that growth of $Al_{1-x}B_xN$ in the wurtzite phase should also be possible. $Al_{1-x}B_xN$ coatings with rather low boron contents are known to already show increased hardnesses and therefore are an interesting field of research. [42]

4.1 Experimental setup

An AJA Orion5 lab scale magnetron sputtering system was used for the deposition of $Al_{1-x}B_xN$ coatings. This system is able to mount one 3" and two 2" targets at a time. In the experimental process boron (B), boron nitride (BN), aluminum (Al) and aluminum diboride (AlB_2) targets were used to figure out the optimal sputtering setup. The AJA sputtering system is able to heat the substrates up to 850°C. Depending on the evacuation time, an ultra-high vacuum ($< 10^{-7}$ mbar) can be established.

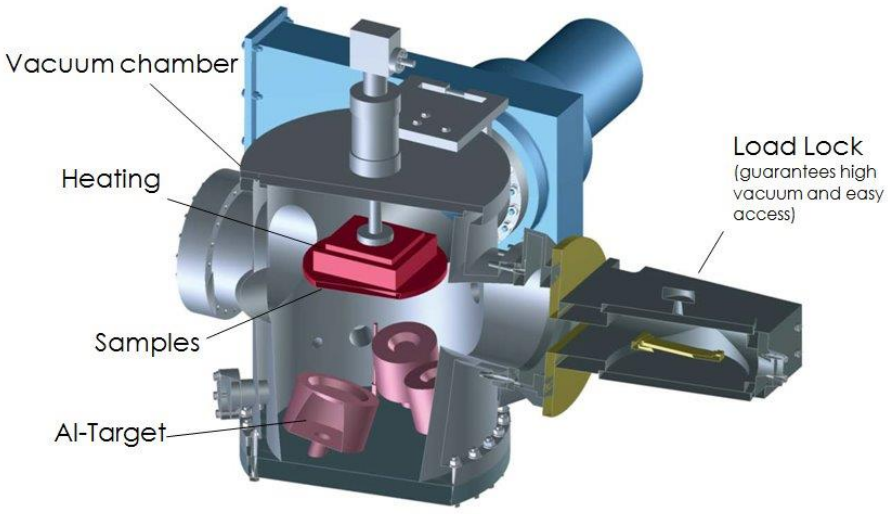

Figure 4.1: AJA Orion5 Lab Scale magnetron sputtering system, showing vacuum chamber, with heating source for the samples, sputtering target and load lock for easy access.

Another advantage of the AJA sputtering system is the load lock with an own vacuum pump, giving the possibility to change the substrates without venting the main chamber. Two ENI RPG plasma generators as well as an AJA DCXS generator were used as power supplies.

Figure 4.12 shows the schematic drawing of the AJA magnetron sputtering system with z being the distance between substrate and end cover of the chamber. Within our group a z distance of 45 mm is known to be advantageous for the deposition of AlN. Therefore, z remains constant at this value for all experiments. In addition, the targets are embedded in a cylinder-shaped chimney with an attached shutter, giving the opportunity to protect the targets surface while being idle and focuses the sputtered material.
To achieve a wide range of compositions, the experiments were carried out with different target currents, controlled by these generators. Single crystalline silicon and austenite wafers were used as substrates and mounted on a rotating substrate holder. Argon and nitrogen were used as process gas. Prior to the deposition process, the substrates were etched for 10 minutes, using a radio frequency generator, with argon as working gas at a pressure of 60 μbar. Etching was performed to activate the surface of the substrate for advanced condensation and crystal growth.

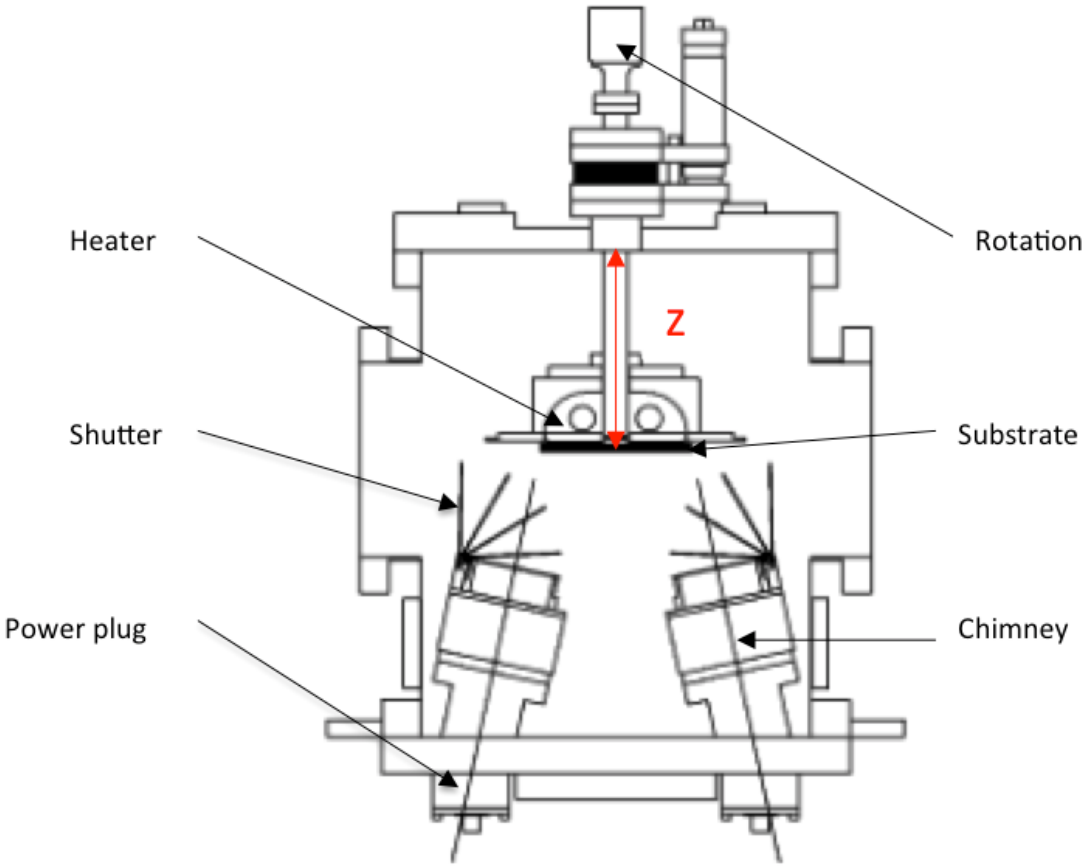

Figure 4.2: Schematic drawing of an AJA sputtering system, showing the rotary substrate holder, heating source, and protective chimneys with shutter to focus the sputtered material. [43]

4.2 Deposition of $Al_{1-x}B_xN$ coatings - 3" Al, 2" B, 300°C

As a first step, a 3" aluminum and a 2" boron target were used to grow $Al_{1-x}B_xN$ coatings. The objective of this setup was to increase the boron content with each deposition. The coatings were deposited on polished and pre-cleaned single crystalline silicon and austenite wafers. While the current on the 2" boron target remained constant at 0.3 A, the current on the 3" aluminum target was increased from deposition to deposition (see Table 1), ranging from 1.0 to 2.0 A.

3" Aluminum					
	AlBN_1	*AlBN_2*	*AlBN_3*	*AlBN_4*	*AlBN_5*
Current $[A]$	2.0	1.8	1.5	1.2	1.0
Voltage $[V]$	220	240	205	175	200
Power $[W]$	438	420	260	210	200
2" Boron					
	AlBN_1	*AlBN_2*	*AlBN_3*	*AlBN_4*	*AlBN_5*
Current $[A]$	0.3	0.3	0.3	0.3	0.3
Voltage $[V]$	300	300	280	310	320
Power $[W]$	90	90	90	95	95

Table 1: Deposition parameters for coatings $AlBN\_1$ to $AlBN\_5$

This should lead to increasing boron contents in the different coatings. Two ENI RPG plasma generators were used as power supplies for the targets. Both targets were operated with pulsed direct current at 150 kHz pulse frequency and with 2576 ns pulse width. The partial pressure of the working gas was kept steady at 4 μbar. The gas flow of argon $f(Ar)$ and nitrogen $f(N_2)$ was set to 5 $sccm$ and 15 $sccm$, respectively. The temperature of the rotating substrate holder was kept at 300 $°C$. These settings were chosen, since they are known to be advantageous for the growth of AlN. Table 2 shows the thickness and the deposition durations for the different coatings. The thickness of the coatings clearly decreases with increasing boron content, which is most likely a result of the current reduction on the Al target, leading to an eased sputtering yield.

Coating thickness					
	AlBN_1	*AlBN_2*	*AlBN_3*	*AlBN_4*	*AlBN_5*
duration $[min]$	150	120	180	120	210
thickness $[\mu m]$	1.73	1.78	1.48	1.05	0.95

Table 2: Thickness and process duration for the coatings $AlBN\_1$ to $AlBN\_5$

4.2.1 EDS

Due to the fact that boron is hardly detectable, a relative high error occurs during EDS analysis, especially for low boron contents. Figure 4.3 shows the EDS spectrum of sample $AlBN\_1$. The boron peak is only slightly visible and cannot clearly be distinguished from the background. This is why boron is not automatically identified by the detection software. The only way to get a result, is to mark the boron position by hand. This problem exists in all low content boron coatings (<5 $at.\%$). Therefore, the chemical composition is not taken into account in this section.

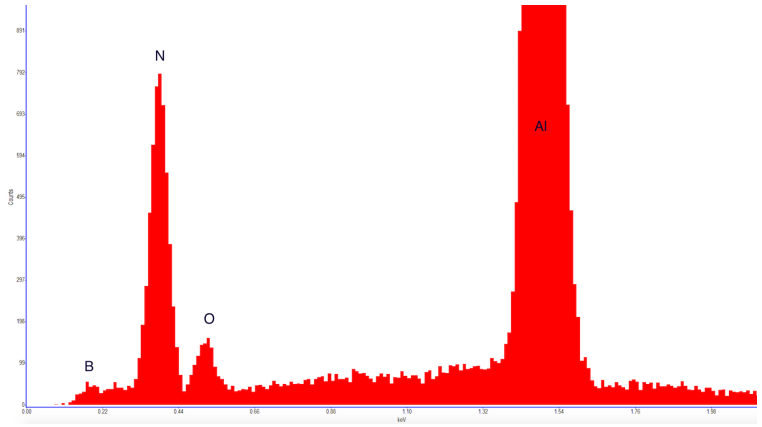

Figure 4.3: EDS spectrum of $AlBN\_1$ with low boron content, including peaks for boron, aluminum and nitrogen.

4.2.2 XRD

Diffraction data were obtained by a PANalytical x-ray diffractometer using grazing incidence diffraction. Grazing incidence is a x-ray diffraction method for identification of crystal structures using a low incidence angle ($\alpha < 3°$), resulting in a low penetration depth. This makes it an ideal method for investigation of thin films. The x-ray diffraction diagram in Figure 4.4 illustrates data from the different depositions discussed in Table 1. Bragg peak positions for w-AlN and h-BN are shown as vertical lines and are marked with the corresponding [hkl]-indices.
Beside AlBN_3 only w-AlN peaks are present in the spectra. A slight peak shift towards higher 2Θ angles can be observed. Due to the mismatch of the lattice constants (see Figure 2.8) of w-AlN and w-BN, this most likely reveals, that boron atoms are included into the aluminum nitride lattice. Another explanation for the peak shift, however, might be residual stress in the crystal lattice. Diffraction peaks between $2\Theta = 54°$ and $58°$ are identified as reflections from the substrate (silicon).
$AlBN\_2$ doesn't show a silicon peak, which may indicate that this film has a higher thickness than the others. With increasing boron content (we expect an increasing boron content due to the increased current), the peaks appear broader, which is a sign for smaller crystallites. Moreover, we see a change of the preferred orientation of w-$Al_{1-x}B_xN$. The preferred orientation at low boron contents ($AlBN\_1/2$) have sharp peaks at $2\Theta = 36°$ and $66°$. These

peaks are identified as stemming from the [002] and the [103] plane of w-AlN. The [103] peak disappears with higher boron content, while the [002] peak becomes less sharp.
In the XRD diagram of $AlBN\_4/5$, we see a variety of peaks indicating a more random crystal orientation. Surprisingly $AlBN\_3$ shows only the substrate peak and a weak signature of a very broad peak at $2\Theta \sim 28°$. This peak is identified as h-BN [002] reflection. The appearance of h-BN together with the more amorphous structure inside the film, makes us expect lower hardnesses.

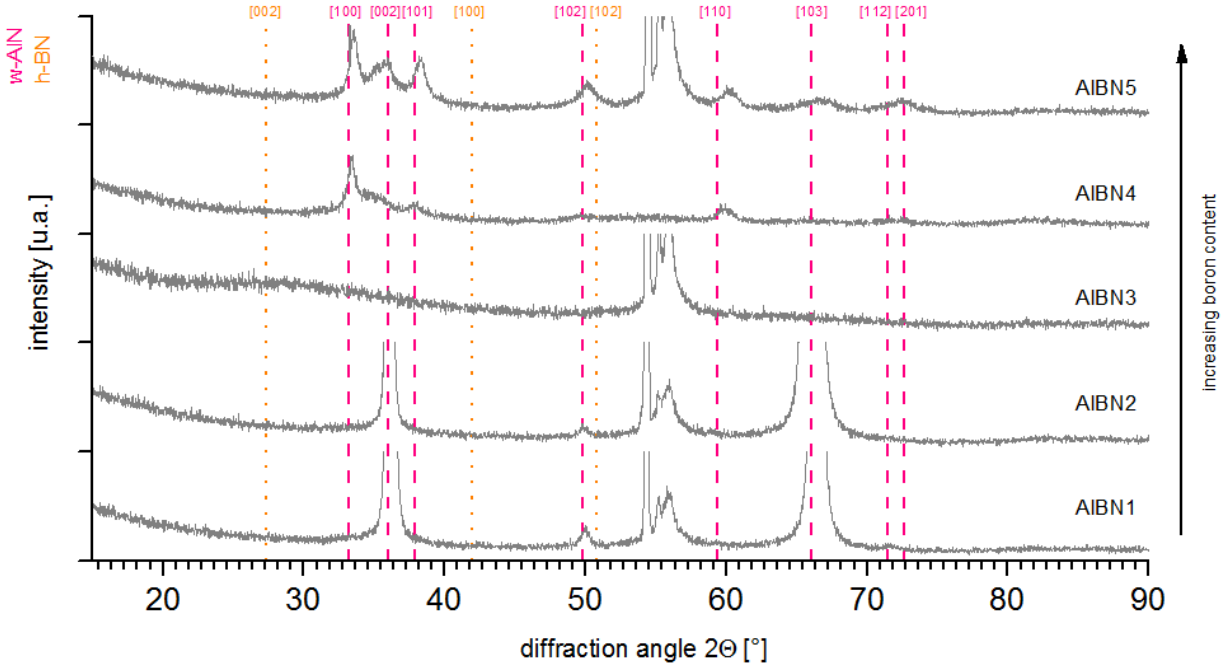

Figure 4.4: Diffraction patterns of thin films containing aluminum, boron and nitrogen. The deposition was performed with a 3" aluminum, a 2" boron target at 300 $°C$ and nitrogen as working gas at 4 μbar. Vertical lines representing Bragg peak positions for w-AlN and h-BN from the ICDD database.

4.2.3 Hardness

The hardnesses of the coatings were determined by an IBIS nanoindentation tester with traceable calibration. The test was carried out with a three sided Berkovich indenter, applying a maximum load of 25 mN with 1 s holding time at various positions on the substrate surface. The average hardnesses were then determined from the unloading curves. Figure 4.5 shows the hardnesses of the $Al_{x-1}B_xN$ coatings $AlBN\_1$ to $AlBN\_5$, ranging from 14 to 29 GPa. Indeed, the lowest hardness coating (14 GPa) is identified as the coating, showing the h-BN peak in the diffraction data. In the literature, the hardness of AlN is stated to be roughly 25 GPa, [2] leading to the conclusion, that the introduction of boron results in a slight raise in hardness. $AlBN\_1$ has the highest hardness, with about 29 GPa. $Al_{1-x}B_xN$ coatings with a preferred crystal orientation, have slight higher hardnesses than coatings with random crystal orientations. Coatings with sharp peaks have larger crystallites, which usually result in lower hardness values.

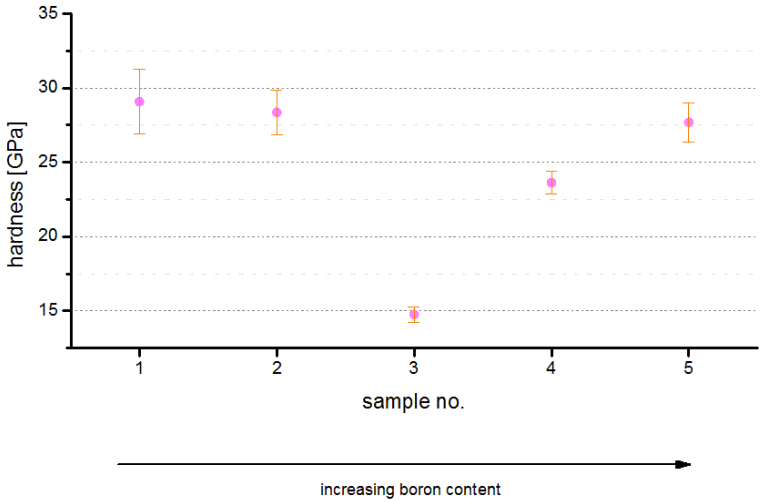

Figure 4.5: Hardnesses of AlBN1 - 5, measured by nanoindentation with an IBIS nanoindentation tester.

4.3 Deposition of $Al_{1-x}B_xN$ coatings - 3" Al, 2" B, 700°C

To investigate the impact of the temperature on the $Al_{1-x}B_xN$ coatings, the next depositions were executed with a rotating substrate holder, which was heated up and kept at 700 $°C$. A 3" aluminum and a 2" boron traget were used for evaporation, with argon and nitrogen as working gases. The gas flow of argon $f(Ar)$ was set to 5 $sccm$ and nitrogen $f(N)$ to 15 $sccm$, while the total pressure in the chamber was kept at 4 μbar, thus keeping the same settings as in previous depositions. Both targets were again operated with pulsed direct current (DC) at 150 kHz pulse frequency and 2576 ns pulse width.

3" Aluminum				
	AlBN_6	*AlBN_7*	*AlBN_8*	*AlBN_9*
Current $[A]$	1.5	1.2	1.0	0.75
Voltage $[V]$	197	156	130	190
Power $[W]$	298	190	130	140
2" Boron				
	AlBN_6	*AlBN_7*	*AlBN_8*	*AlBN_9*
Current $[A]$	0.2	0.2	0.2	0.2
Voltage $[V]$	245	344	340	330
Power $[W]$	72	71	71	64

Table 3: Deposition parameters for coatings $AlBN\_6$ to $AlBN\_9$

To achieve an increasing boron content, the current on the aluminum target was decreased from 1.5 to 0.75 A, in four subsequent deposition runs. The current on the boron target remained constant at 0.2 A for every deposition. Table 3 shows the parameters for the depositions $AlBN\_6$ to $AlBN\_9$. We expect an increasing boron content with decreasing current. The current reduction also leads to a decrease in sputtering yield, which directly affects the thickness of the coatings (see Table 4).

Coating thickness				
	AlBN_6	*AlBN_7*	*AlBN_8*	*AlBN_9*
duration $[min]$	180	180	180	240
thickness $[\mu m]$	1.41	0.58	0.28	0.45

Table 4: Thickness and process duration for the coatings $AlBN\_6$ to $AlBN\_9$

4.3.1 EDS

Figure 4.6 shows the EDX spectrum of the sample *AlBN_7*. As described in section 4.2.1, boron is very difficult to detect with this method. Furthermore, the boron peak is not automatically identified by the detection software and has to be classified by the user.

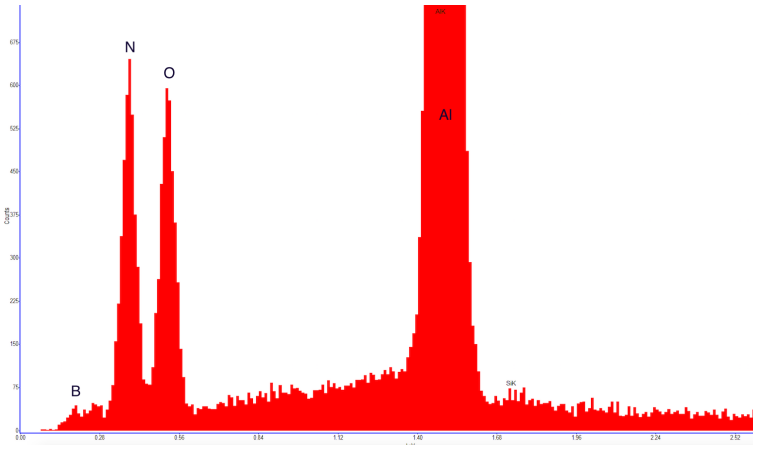

Figure 4.6: EDX spectrum of *AlBN_7* with peaks identified as aluminum, oxygen, nitrogen and boron.

Especially small boron contents cannot be filtered accurately from the background. In our case, it seems like that this problem is only related to setups with a 3" Aluminum and a 2" boron target. Samples *AlBN_6* to *AlBN_9* show small and hardly visible boron peaks and therefore an exact determination was not possible. These depositions can be estimated to most likely have a boron content below 5 *at.%*.

4.3.2 XRD

The diffraction diagram in Figure 4.7 shows data of four different depositions, with the Bragg peak positions for w-AlN and h-BN as vertical lines and the corresponding [hkl]-indices. XRD peaks between $2\Theta = 52°$ and $58°$ are, as previously discussed, identified as reflections from the silicon substrate. The peak shift towards higher 2Θ angles is an indicator, that boron atoms are included into the aluminum nitride lattice. Another explanation for the peak shift, especially for shifts towards lower 2Θ angles (*AlBN_8/9*), may be the introduction of residual stress in the crystal lattice during the deposition process. This is related to the mismatch of lattice constants of substrate and coating, and may be enhanced by higher deposition temperatures. At low boron contents (*AlBN_6*) we see several sharp peaks in the diffraction diagram, which indicate large crystallites in the coating. With increasing boron content the peaks either broaden and decrease in intensity or disappear completely. This is due to the crystallites becoming smaller and loosing their preferred orientation. Moreover, the coatings with higher boron content get progressively more amorphous.

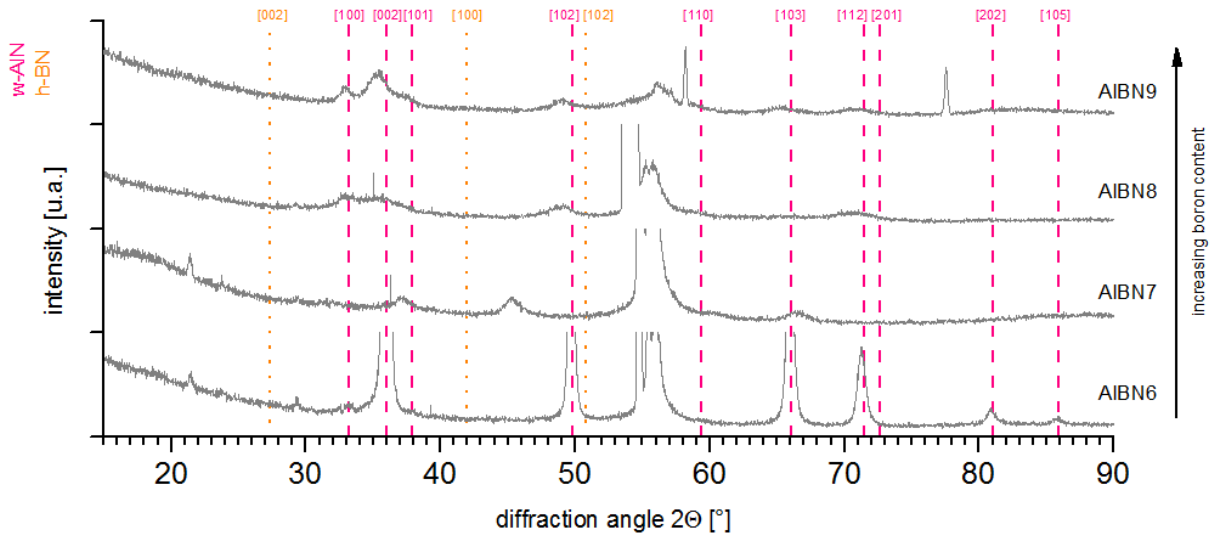

Figure 4.7: Diffraction patterns of thin films containing aluminum, boron and nitrogen. The deposition was performed with a 3" aluminum and a 2" boron target at 700 $°C$ and nitrogen as working gas at 4 μbar. Vertical lines represent Bragg peaks for w-AlN and w-BN from the ICDD database.

4.3.3 Hardness

Hardnesses of the samples $AlBN\_6$ to $AlBN\_9$ are illustrated in Figure 4.8. The hardness was determined by nanoindentation, using a three-sided Berkovich indenter with a maximum load of 25 mN and 1 s holding time. Within the limit of accuracy of the measurements, the hardness does not change significantly for the different deposition runs. This seems to indicate that, with this setup, it was not possible to get much boron into the coatings. As in the previous section, the coatings with preferred orientation ($AlBN\_6/7$) show the highest hardness. Again, the effect of smaller grains seems to be balanced by the loss of the preferred orientation and even results in a decrease in hardness towards 20 GPa ($AlBN\_7/8$).

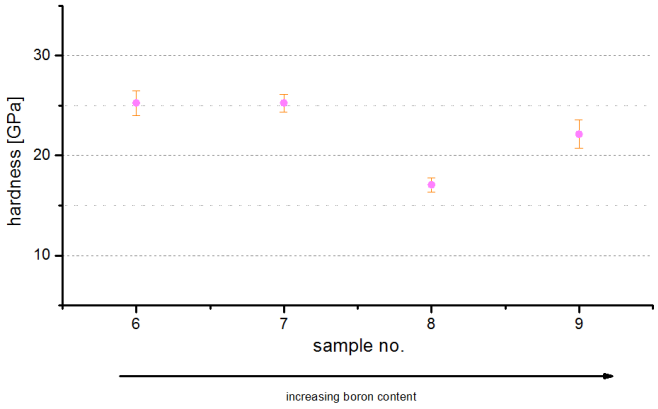

Figure 4.8: Hardness of the samples $AlBN\_6$ to $AlBN\_9$ determined by nanoindentation

4.4 Deposition of $Al_{1-x}B_xN$ coatings - 3" B, 2" Al, 300°C

Since previous configurations were not able to grow films, with boron contents exceeding ∼10 *at.*%, in this configuration, a 3" boron target and a 2" aluminum target were used for the deposition. While the current on the 2" aluminum target was kept at 0.8 A, the current on the boron target was increased with each deposition, starting at 0.2 A. Due to the poor conductivity of the 3" boron target, it had to be powered by a pulsed direct current with a pulse frequency of 150 kHz and a pulse width of 2576 ns. The aluminum target was operated at direct current. Both targets were powered by an ENI RPG plasma generator. As before, Argon and nitrogen were used as working gases, with a total pressure of 4 μbar inside the chamber. The gas flow of argon $f(Ar)$ was set to 5 $sccm$ and nitrogen $f(N_2)$ to 15 $sccm$. Pre-cleaned single crystalline silicon and austenite were used as substrate for the coatings. The temperature of the substrates was kept at 300 $°C$. The settings of the different deposition runs are shown in Table 5.

3" Boron					
	AlBN_10	*AlBN_11*	*AlBN_12*	*AlBN_13*	*AlBN_14*
Current $[A]$	0.2	0.3	0.5	0.9	1.1
Voltage $[V]$	250	310	306	261	280
Power $[W]$	50	94	150	235	305
2" Aluminum					
	AlBN_10	*AlBN_11*	*AlBN_12*	*AlBN_13*	*AlBN_14*
Current $[A]$	0.8	0.8	0.8	0.8	0.8
Voltage $[V]$	470	370	320	275	290
Power $[W]$	360	290	250	221	225

Table 5: Deposition parameters for the coatings $AlBN$_10 to $AlBN$_14

Table 6 shows the thickness of the different coatings as well as the duration of each deposition. As it is shown in previous sections, the thickness depends on the sputtering yield, which is directly affected by the current on the targets. With increasing current on the boron target, we see a raise in thickness to a maximum of 2.3 μm (sample $AlBN$_14).

Coating thickness					
	AlBN_10	*AlBN_11*	*AlBN_12*	*AlBN_13*	*AlBN_14*
duration $[min]$	180	180	180	140	180
thickness $[\mu m]$	0.85	1.05	1.1	2.14	2.3

Table 6: Thickness and duration for the coatings $AlBN$_10 to $AlBN$_14

4.4.1 EDS

Table 7 shows the chemical composition of the samples $AlBN$_10 to $AlBN$_14. The compositions were determined by energy dispersive x-ray spectroscopy, using a scanning electron microscope. The boron content for the depositions discussed above, is high enough for a

valid declaration and therefore used in this section. As expected, the EDS results show an increasing boron content in the coatings, while the aluminum content decreases with each deposition. Therefore, the purpose of the setup, to increase the boron content, was fulfilled.

sample no.	**B [at.%]**	**Al [at.%]**	**N [at.%]**
$AlBN\_10$	9	51	50
$AlBN\_11$	16	31	52
$AlBN\_12$	26	18	56
$AlBN\_13$	36	8	55
$AlBN\_14$	42	4	54

Table 7: Chemical compositions for samples $AlBN\_10$ to $AlBN\_14$ determined by energy dispersive x-ray spectroscopy

4.4.2 XRD

Figure 4.9 shows the diffraction digram of the coatings $AlBN\_10$ to $AlBN\_14$. Vertical lines represent the Bragg peak positions for w-AlN and h-BN, marked with the corresponding [hkl]-indices.

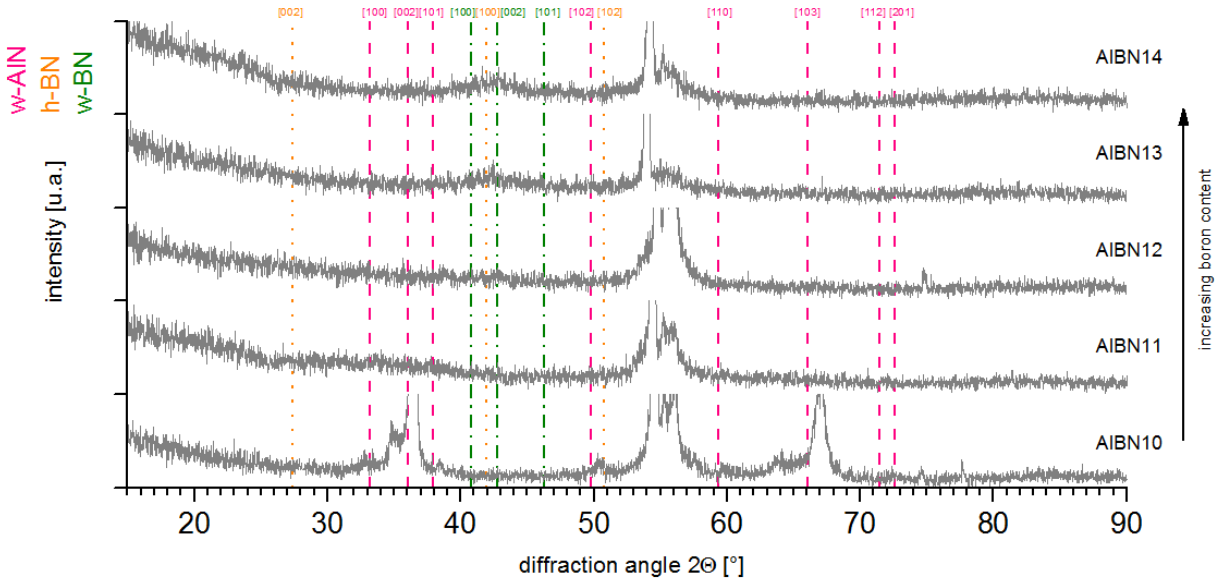

Figure 4.9: Diffraction patterns of thin films containing aluminum, boron and nitrogen. The deposition was performed with a 2" aluminum and a 3" boron target at 300 $°C$ with argon and nitrogen as working gas at 4 μbar. Vertical lines represent Bragg peaks of w-AlN and h-BN from the ICDD database.

While the peaks at $2\Theta = 33°$, 36° and 50.5° can be identified as stemming from w-$Al_{1-x}B_xN$, with rather low boron content (slight shift towards higher 2Θ angles), the peaks at $2\Theta = 35°$ and 64° have a different origin. Due to the significantly smaller lattice parameters of w-BN,

the corresponding Bragg reflections are to be found at strongly increased 2Θ angles. For example, [100] of w-AlN at 35° shifted to about 41° in w-BN. Therefore, a high boron content is likely to lead to a significant shift towards higher 2Θ angles. Thus we can identify the peaks at 2Θ = 35° and 64°, as [100] and [110] reflections of a boron rich w-$Al_{1-x}B_xN$. This means that the $AlBN$_10 coating contains two w-$Al_{1-x}B_xN$ phases, with different boron contents. Peaks between 2Θ = 52° and 58° are identified as reflections from the silicon substrate. With increasing boron content the w-AlN reflections disappear, which is an effect of the coating getting amorphous. $AlBN$_14 shows a very broad reflection at 2Θ ∼ 43°. This reflection is identified as h-BN peak with the orientation [100]. We assume, that in $Al_{x-1}B_xN$ coatings, the w-AlN phase only exists at very low boron contents (<10 $at.\%$). Above this critical value the h-BN phase is present or the coatings become amorphous.

4.4.3 Hardness

Figure 4.10 shows hardnesses versus the boron contents of the samples $AlBN$_10 to $AlBN$_14. The hardnesses were determined by nanoindentation using a three-sided Berkovich indenter. Maximum load of the test was 25 mN at 1 s holding time.
The hardness decreases significantly with increasing boron content, which is related to the disappearing of the wurtzite structure and amorphization of the coatings. At a boron content of about 9 $at.\%$ the coating is still crystalline, consisting of two $Al_{1-x}B_xN$ phases with different boron contents, which results in a hardness value of 29 GPa. With further increasing boron content the structure gets amorphous, resulting in an strong decrease in hardness. At a boron content of 32 $at.\%$ ($AlBN$_14) a hardness of 7 GPa was determined, which is a significant lower as compared to $AlBN$_10. The hardness of $AlBN$_10, is the highest value, that could be obtained in this work. A further increase in the boron content leads to amorphisation or formation of small h-BN crystallites. This clearly results in a significant reduction of hardness.

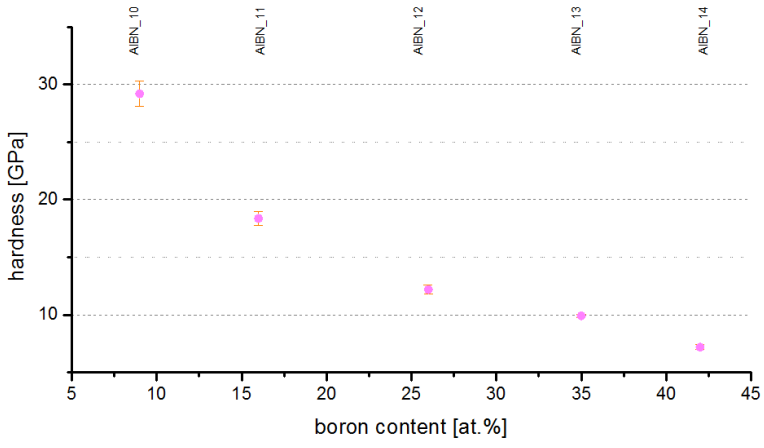

Figure 4.10: Hardness versus boron content of the samples $AlBN$_10 to $AlBN$_14

4.5 Heat treatment- 3" boron, 2" aluminum, 300 °C - 700 °C 30 min.

Due to the amorphous character of the coatings in section 4.4, a heat treatment of the samples $AlBN\_10$ to $AlBN\_14$ was performed. This way, the coatings might crystallize, due to the additional energy provided, which leads to diffusion processes. The results of the XRD and hardness tests are then compared to the coatings in the original condition. A Centorr high temperature vacuum furnace was used for the heat treatment. The samples were heated for 30 *mins* at 700 $°C$

4.5.1 XRD

The diffraction diagrams of the coatings $AlBN\_10$ to $AlBN\_14$ are shown in Figure 4.11. Within the diagrams vertical lines represent the Bragg peak positions for w-AlN and h-BN, which are marked with the corresponding [hkl]-indices.

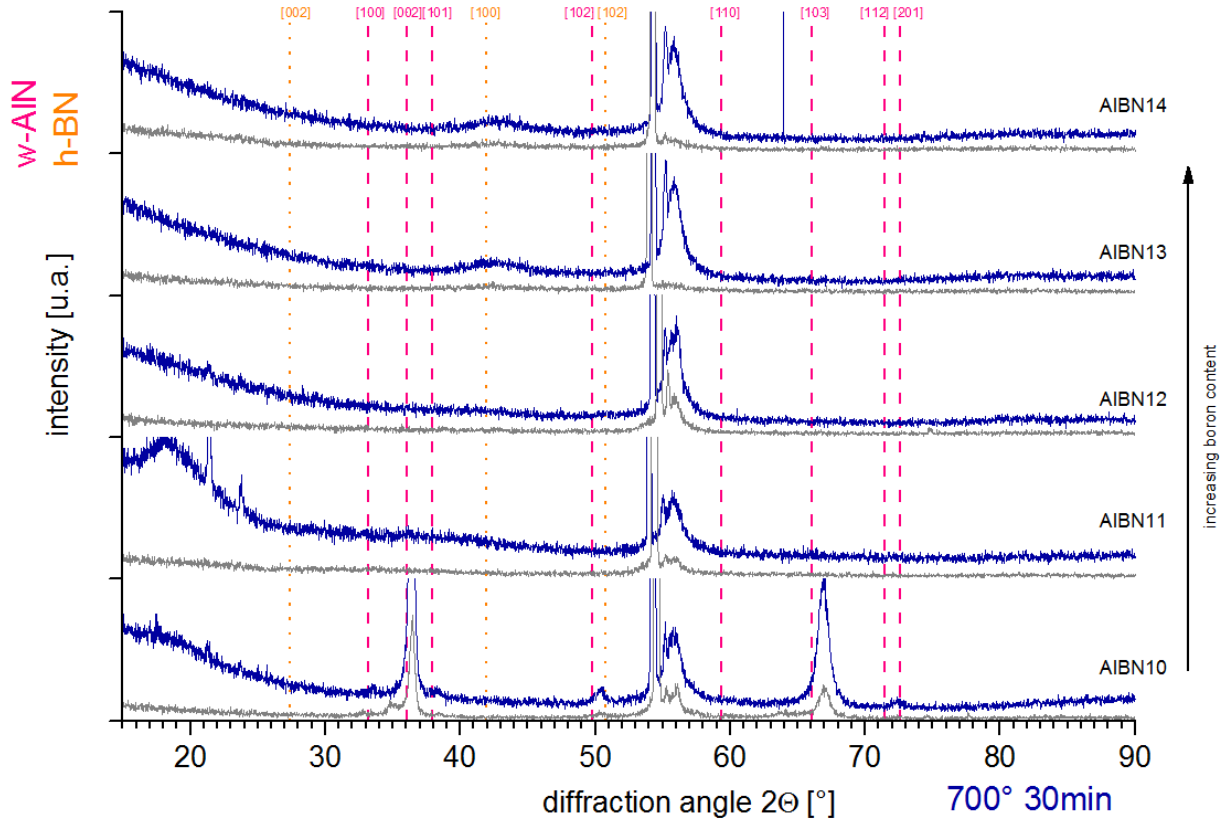

Figure 4.11: Comparison of the coatings $AlBN\_10$ to $AlBN\_14$ before and after annealing (for deposition conditions see Table 7). Vertical lines represent Bragg peaks from the ICDD database. Heat treatment was executed for 30 *min* at 700$°C$.

After the heat treatment, the peaks at $2\Theta \sim 36°$ and 67° of the low boron content sample ($AlBN\_10$), develop much higher intensities and the reflections from the boron rich w-$Al_{1-x}B_xN$ can not be detected anymore. This suggests, that the Al-rich wurtzite structured $Al_{x-1}B_xN$ and B-rich wurtzite structured $Al_{x-1}B_xN$ phases intermix. At boron contents higher than ∼9 $at.\%$, no significant change in the diffraction diagrams can be observed, meaning that no crystallization was induced ($AlBN\_11$ and $AlBN\_12$). The samples remain amorphous in the XRD pattern. Boron contents over 36 $at.\%$ show a very broad and flat peak at $2\Theta \sim 42°$, which is identified as a reflection of the [100] plane of the h-BN crystal structure.

4.5.2 Hardness

Table 8 shows the hardnesses of the coatings $AlBN\_10$ to $AlBN\_14$, before and after the heat treatment. Hardnesses were determined by nanoindentation using a three-sided Berkovich indenter. Maximum load of the test was 25 mN at 1 s holding time.
We see a decrease in hardness with increasing boron content, which is related to the amorphous crystal structure, beginning at a boron content of about 10 $at.\%$. As mentioned before, hardnesses of $Al_{x-1}B_xN$ coatings are strongly dependent on the presence of the w-AlN crystal structure. With proceeding amorphization, the hardness drops significantly. After annealing, the hardness of the samples was measured again with the same configuration. Surprisingly the hardness of sample $AlBN\_10$ didn't change within the limits of accuracy, although the morphology changed from a coating composed of Al-rich and B-rich w-$Al_{x-1}B_xN$ phases to a coating composed of more or less homogeneous w-$Al_{x-1}B_xN$ phases.

sample no.	**hardness [GPa]**	**hardness [GPa]** **700**$°C$ **30** min
$AlBN\_10$	29.18 ± 1,09	27.84 ± 0.73
$AlBN\_11$	18.36 ± 0,58	20,09 ± 0.42
$AlBN\_12$	12.18 ± 0,41	12.44 ± 0.42
$AlBN\_13$	8.28 ± 0.36	8.02 ± 0.31
$AlBN\_14$	7.18 ± 0.22	7.82 ± 0.33

Table 8: Hardnesses of the samples $AlBN\_10$ to $AlBN\_14$, before and after the heat treatment.

4.6 Development of $Al_{1-x}B_xN$ coatings with a combinatorial setup

Another approach, to achieve different boron contents in the coatings is, to prevent the substrate holder from rotating. This way the distribution of the elements is mainly effected by the position of the targets with respect to the substrates. Substrates that are positioned directly over a specific target, will most likely have the highest content of this targets element. The targets are arranged in a triangle-like shape, with boron being in one corner, clockwise followed by aluminum and aluminum diboride. In our case, this setup includes a 3" boron, a 2" aluminum and a 2" aluminum diboride target. Table 9 shows the adjustments on the different targets, that were powered by two ENI RPG plasma generators (B, Al) and an AJA DCXS (AlB_2).

Parameters for no substrate rotation			
Target	Current $[A]$	Voltage $[V]$	Power $[W]$
3" Boron	0.5	260	**133**
2" Aluminum	0.8	140	**113**
2" Aluminum diboride	0.3	460	**144**

Table 9: Deposition parameters for the coatings prepared without substrate rotation

To receive a maximum of analyzable data with a high boron distribution, 14 pre-cleaned and polished single crystalline silicon wafers were placed in the substrate holder. The substrate holder was kept at a temperature of 500 $°C$ and the duration of the deposition was 240 min. Previous to the deposition process, the substrates were etched with a radio frequency generator at 25 W for 10 $mins$, with argon as working gas. While the boron and the aluminum target were operated at direct current at a pulse width of 2576 ns and a pulse frequency of 150 kHz, the AlB_2 target was operated with a direct current. Argon (Ar) and Nitrogen (N_2) were used as working gases, with gas flows of $f(Ar)$=5 $sccm$ and $f(N_2)$=15 $sccm$. The total pressure of the working gases was set to 4 μbar.

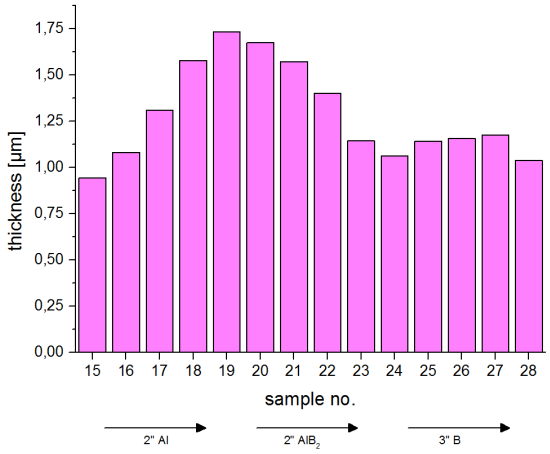

Figure 4.12: Thicknesses and approximate positions of the coatings prepared without substrate rotation.

Contrary to previous sections, the deposition parameters for the coatings $AlBN\_15$ to $AlBN\_28$ did not change, but the positions of the individual substrates above the different cathodes are distinct. The thicknesses of the coatings have the highest values at the position between the Al and the AlB_2 target. Based on the lower sputter yield of B with respect to Al and AlB_2, the coatings above the B target are thinner, although the B target is larger with 3" than the 2" Al and AlB_2 targets.

4.6.1 XRD

The x-ray diffraction diagrams of the resulting coatings are shown in Figure 4.14. Bragg peak positions of w-AlN and h-BN are represented by vertical lines, which are marked with the corresponding [hkl]-indices. The coating with the highest boron content should be $AlBN\_20$, as it was positioned directly over the 3" boron target. With increasing sample number, the boron content should decrease due to the increasing distance to the 3" boron target.
The XRD diagrams show the typical peaks for the silicon substrate between $2\Theta = 52°$ and 58°. For several samples, we see a peak at $2\Theta \sim 43°$, which is identified as a reflection of the [100] plane of h-BN crystal structure. The formation of h-BN might refer to a high boron content at high temperatures like it is reviewed in previous sections. All in all, it was not possible to achieve a growth of the w-AlN crystal structure with this setup.

4.6.2 Hardness

Hardnesses of the coatings with disabled substrate rotation were determined by nanoindentation. The four Samples, that represent the approximate boron distribution for all coatings, were picked for analyzing. The test was fulfilled using a three-sided Berkovich indenter with a maximum load of 25 mN at 1 s holding time. The diagram (Fig 4.13) shows the hardnesses of the samples $AlBN\_16$, $AlBN\_19$, $AlBN\_23$ and $AlBN\_26$. As it was discussed in the previous sections, the hardnesses of $Al_{x-1}B_xN$ coatings are strongly dependent on the existence of the w-AlN phase. The XRD diagrams do not show these reflections, which may beforehand lead to the assumption, that the coatings have low hardnesses (compared to coatings with w-AlN crystal structure). As it is shown in Figure 4.13, the hardnesses of the samples range from ~7 to 11 GPa, which is in fact a low value, compared to the maximum hardness of 29 GPa from the coatings with sharp w-AlN peaks.

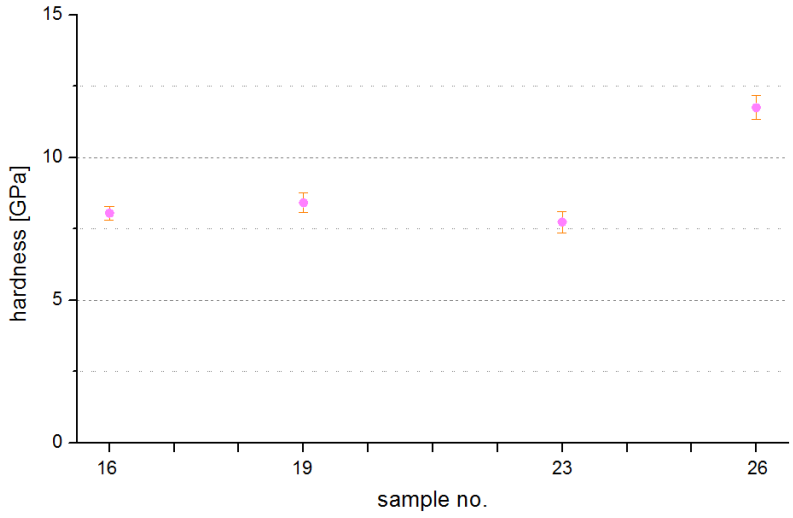

Figure 4.13: Hardnesses of the samples $AlBN\_16$, $AlBN\_19$, $AlBN\_23$ and $AlBN\_26$, representing the hardness distribution of the coatings prepared without substrate rotation.

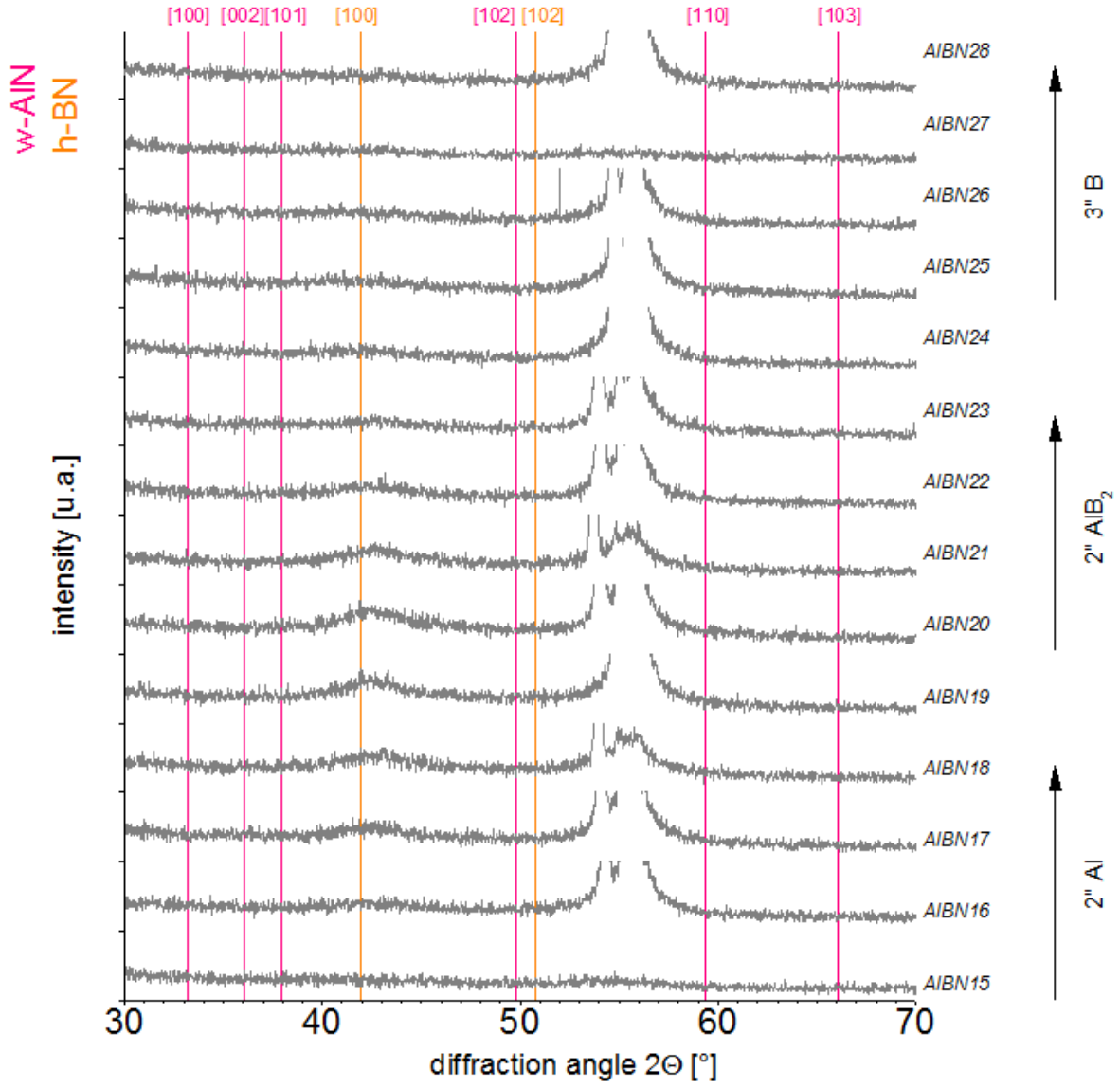

Figure 4.14: Diffraction patterns the coatings with no substrate rotation, containing aluminum, boron and nitrogen. The deposition was performed, using non rotating substrate holder at 500 $°C$ and three different targets, including a 2" aluminum, a 3" boron and a 2" AlB_2 target. Argon and nitrogen served as working gases at a partial pressure of 4 μbar. Vertical lines represent Bragg peaks from the ICDD database.

5 Summary and conclusion

In this work structural and mechanical properties of $Al_{x-1}B_xN$ coatings with different Al, B and N contents were analyzed by XRD, EDS and nanoindentation. The coatings were deposited by physical vapor deposition with different target setups at various substrate temperatures.
The XRD data revealed, that is was not possible to grow $Al_{x-1}B_xN$ coatings in the wurtzite phase, with B contents exceeding the critical content of 10 $at.\%$. Below this critical value, the coatings show reflections, corresponding to w-AlN with slight peak shifts. These shifts may be used as an indicator for B being included into the w-AlN crystal lattice, due to the mismatch of the lattice constants of w-AlN and w-BN. The coatings are less preferred oriented with increasing B content (>10 $at.\%$), resulting in XRD patterns indicative for an amorphous character.
Nanoindentation measurements of the $Al_{x-1}B_xN$ samples have shown, that the hardnesses of the coatings significantly decrease with B contents above 10 $at.\%$. The $Al_{x-1}B_xN$ coating with around 10 $at.\%$ B content exhibits the highest hardness among all coatings studied (29 GPa). Higher B containing coatings develop an XRD amorphous structure, where even indications for h-BN could be detected. Therefore, these coatings show significantly lower hardness values, which are only 7 GPa for the coating with 46 $at.\%$ B. Even after a 30 min annealing treatment at 700 $°C$, no significant change in hardness (or structure) could be detected, which points towards a high thermal stability of these materials.

List of Figures

List of Tables

References

[1] Z. Pan, H. Sun, Y. Zhang, C. Chen: Harder than Diamond: Superior Indentation Strength of Wurtzite BN and Lonsdaleite, Physical Review Letters 102 (2009)

[2] Y. Yang, C. Chang, Y. Hsiao, J. Lee, B. Lou: Influence of high power impulse magnetron sputtering pulse parameters on the properties of aluminum nitride coatings, Surface and Coatings Technology (2014)

[3] J. Davis: Surface Engineering for Corrosion and Wear Resistance, ASM International, Materials Park, (2001)

[4] P. M. Martin: Handbook of deposition technologies for thin films and coatings, Elsevier Inc., Burlington, (2010)

[5] A. Liu, M. Cohen: Prediction of New Low Compressibility Solids, Science Vol. 245 (1989), pp. 841 - 842

[6] R. Kaner, J. Gilman, S. Tolbert: Designing Superhard Materials, Science Vol. 308 (2005), pp. 1268-1269

[7] N. Dubrovinskaia, V. Solozhenko, N. Miyajima, V. Dmitriev, O. Kurakevych, L. Dubrovinsky: Superhard nanocomposite of dense polymorphs of boron nitride: Noncarbon material has reached diamond hardness, Applied Physics letter Vol. 90 (2007)

[8] Donald M. Mattox: Handbook of Physical Vapor Deposition, 2nd Edition, Elsevier Inc., 2010

[9] W. D. Westwood, Sputter deposition (AVS Education Committee book series, New York 2003)

[10] K.Wasa, I. Kanno, H. Kotera: Handbook of Sputter Deposition Technology, 2nd Edition, Park Ridge, NJ : Noyes Publ., 1992

[11] Milton Ohring: Materials Science of Thin Films, 2nd Edition, Acad. Press., San Diego, (2007)

[12] W.D. Callister Jr., D.G. Rethwisch: Fundamentals of Materials Science and Engineering, 3rd Edition, John Wiley and Sons, Inc., (2008)

[13] I. Petrov, P. B. Barna, L. Hultman, J. E. Greene: Microstructural evolution during film growth, Journal of Vacuum Science and Technology A21 (2003), pp. 117

[14] P.B. Barna, M.Adamik: Fundamental structure forming phenomena of polycrystalline films and the structure zone models, Thin Solid Films A317 (2008), pp. 27-33

[15] P.B. Barna, M. Adamik, in: F.C. Matacotta, G. Ottaviani ZEds., Science and Technology of Thin Films World Scientific Publ., Singapore, (1995), 1

[16] M. Adamik, P.B Barna, I. Tomov, D. Biro, Phys. Status Solidi A145 (1994), pp. 275

[17] W. Ensinger, M. Kiuchi: Ion Implantation Technology Proceedings, 1998 International Conference on. S1033-1035 vol.2

[18] B.A. Movchan, A.V. Demchishin, Fiz. Met. A28 (1969) pp. 83

[19] N. N. Greenwood and A. Earnshaw: Chemistry of the elements, Oxford (1995)

[20] Y. Taniyasu, M. Kasu T. Makimoto: An aluminium nitride light-emitting diode with a wavelength of 210 nanometres, Nature A441 (2006), pp. 325-328

[21] K.Momma, F. Izumi: VESTA: a three-dimensional visualization system for electronic and structural analysis, J. Appl. Cryst. (2008) 41, 653-658

[22] R.G. Delaplane, U. Dahlborg, B. Graneli, P. Fischer, T. Lundstrom, A neutron diffraction study of amorphous boron, Journal of Non-Crystalline Solids A104 (1988), pp. 249

[23] Y.G. Gogotsi R.A. Andrievski: Materials Science of Carbides, Nitrides and Borides, Springer, (1999)

[24] M. Kawaguchi, S. Kuroda, Y. Muramatsu: Journal Of Physics And Chemistry Of Solids, A69 (2008), pp.1171-1178

[25] J. Xu, L. Yu, S. Dong, I. Kojima: tructure transition of BN layers and its influences on the mechanical properties of AlN/BN nanomultilayers, Thin Solid Films 516 (2008), pp. 8640-8645

[26] J.H. Edgar, D.T. Smith, C.R. Eddy Jr., C.A. Carosella, B.D. Sartwell, Thin Solid Films 298 (1997) 33.

[27] W. Seidel: Werkstofftechnik, 7. Auflage, Hanser Verlag

[28] H.J. Bargel, G. Schulze: Werkstoffkunde, Springer, (2008)

[29] S. Kim, E. Jeon, D. Kwon: Determining Brinell Hardness From Analysis of Indentation Load-Depth Curve Without Optical Measurement, J. Eng. Mater. Technol. 127 (2005), pp. 154-158

[30] L.D. Hanke: Handbook of Analytical Methods for Materials, Materials Evaluation and Engineering, Inc. (2010)

[31] A.C. Fischer-Cripps: Nanoindentation, 2nd edR, Springer-Verlag, N-Y, 2004.

[32] A.C. Fischer-Cripps: Critical review of analysis and interpretation of nanoindentation test data, Surface and Coatings Technology 200 (2006), pp. 4153-4165

[33] C.A. Schuh, Nanointendation studies of materials, Materials Today 9 (2006), pp. 5

[34] W.C. Oliver, G.M. Pharr: Measurement of hardness and elastic modulus by instrumented indentation: Advances in understanding and refinements to methodology, J. Mater. Res., Vol. 19 (2004)

[35] W.C. Oliver and G.M. Pharr, J. Mater. Res. 7 (1992), pp. 1564

[36] H. Stanjek, W. Häusler: Basics of x-ray diffraction, Hyperfine Interactions 154 (2004), pp. 107 - 119

[37] W. H. Bragg, W. L. Bragg: The Reflection of X-rays by Crystals, Proceedings of the Royal Society of London 88 (1913), pp. 428-438

[38] L. Spiess, G. Reichert, R. Schwarzer, H. Behnken, C. Genzel: Moderne Röntgenbeugung, Vieweg (2009)

[39] V. Holy, U. Pietsch, T. Baumbach: High Resolution X-Ray Scattering from Thin Films and Multilayers, Springer (1998)

[40] Noran Instruments: Energy Dispersive X-Ray Microanalysis: An Introduction, Noran Instruments Inc., Middleton (1999)

[41] H. Marihart: TaN Relation Pulsed versus HIPIMS, Diploma Thesis (2015)

[42] L. Liljeholm, M. Junaid, T. Kubart, J. Birch, L. Hultman, I. Katardjiev: Synthesis and characterization of (0001)-textured wurtzite $Al_{1-x}B_xN$ thin films, Surface and Coatings Technology 206 (2011) 1033-1036

[43] AJA International Inc.: http://www.ajaint.com/systems_orion.htm